ELSEVIER

Contents lists available at ScienceDirect

Global and Planetary Change

journal homepage: www.elsevier.com/locate/gloplacha



Records of chemical weathering and volcanism linked to paleoclimate transition during the Late Paleozoic Icehouse

Dawei Lv ^a, Luojing Wang ^a, John L. Isbell ^b, Changyong Lu ^c, Pingping Li ^a, Yujia Wang ^a, Zhihui Zhang ^a, ^{*}

- ^a Shandong Provincial Key Laboratory of Depositional Mineralization and Sedimentary Minerals, College of Earth Sciences and Engineering, Shandong University of Science and Technology, Oingdao 266590, China
- ^b Department of Geosciences, University of Wisconsin-Milwaukee, 3209 N. Maryland Avenue, Milwaukee, WI 53211, USA
- ^c Shandong Provincial Research Institute of Coal Geology Planning and Exploration, Jinan 250104, China

ARTICLE INFO

Editor: Dr. Maoyan Zhu

Keywords: Late Paleozoic icehouse Paleoclimate Taiyuan Formation Volcanism

ABSTRACT

The late Paleozoic ice age (LPIA) was the longest-lived glaciation of the Phanerozoic, and the demise of LPIA is the Earth's only recorded transition from an icehouse to a greenhouse state. In order to explore the records of chemical weathering and volcanism linked to paleoclimate, an integrated multi-proxy study from the Pennsylvanian to the earliest Cisuralian in the Western Shandong from the North China Craton (NCC) was conducted, including results of chemical weathering induces (CIA, CIW, PIA, WIP, CIX, and τ_{Na}), element indicators (Sr/Ba, Sr/Cu, and Rb/Sr), Hg concentration, total organic carbon (TOC), and organic carbon isotope ($\delta^{13}C_{org}$). The chemical weathering indies show a peak of chemical weathering intensity during the early Asselian (~298 Ma), indicating a warming event occurred at that time. Hg/TOC shows one obvious peak of volcanic intensity, corresponding with the rapid increase of chemical weathering. Moreover, the peak in volcanic intensity coincides with negative excursions of $\delta^{13}C_{org}$, hinting at volcanic drivers for the perturbations of carbon isotope and the change of paleoclimate. This phenomenon coincides with the change of conodont oxygen isotope (δ^{18} O), a shift in atmospheric partial pressure of CO₂ (pCO₂), sea-level variation, and late Paleozoic deglaciation records that together document the earliest Permian climate warming-cooling perturbation with a temperature maximum. We suggest that the climate warming in the early Asselian may be driven by volcanism through released greenhouse gas. Our result provides an important contribution to enabling the correlation of volcanic and climatic events during glacial and interglacial cycles.

1. Introduction

The late Paleozoic icehouse is the most serious glaciation in the Phanerozoic (Isbell et al., 2003; Horton et al., 2007; Fielding et al., 2008; Isbell et al., 2012; Montañez et al., 2016; Isbell et al., 2021). The late Paleozoic ice age (LPIA) records the only transition from a greenhouse to an icehouse with complex terrestrial ecosystems to a full greenhouse world, beginning in the Famennian and ending in the Wuchiapingian, spanning ~106 million years (Isbell et al., 2021; Rosa and Isbell, 2021). Multiple episodes of glacial expansion and interglacial shrinkage occurred in the late Paleozoic ice age (Isbell et al., 2003; Fielding et al., 2008; Gulbranson, 2011; Metcalfe et al., 2015; Griffis et al., 2019; Griffis et al., 2021; Dietrich et al., 2021; Le Heron et al., 2021; Sun et al., 2022). Many studies focused on the records of carbonate rocks and marine

biological fossils to reconstruct sea level (Miller et al., 2005; Haq and Schutter, 2008), biodiversity (Gastaldo et al., 1996; Shen et al., 2006; Davydov, 2014; Groves and Wang, 2013; Groves and Yue, 2009), stable-isotope excursions (Korte et al., 2005; Grossman et al., 2008; Isozaki et al., 2007; Chen et al., 2013; Chen et al., 2018; Chen et al., 2022), change of paleotemperature (Yang et al., 2014; Yang et al., 2016), paleofires and atmospheric oxygen levels (Shao et al., 2012; Yan et al., 2019). Some studies proved a further coupling of atmospheric partial pressure of CO₂ (pCO₂) and surface temperatures with changing global ice volume during the LPIA (Montañez et al., 2016; Richey et al., 2020; Isbell et al., 2021; Lu et al., 2021; Chen et al., 2022). Recently, volcanism has been considered a causal mechanism for the increasing atmospheric pCO₂ and changing the global climate in the Paleozoic (Soreghan et al., 2019; Yang et al., 2020; Lu et al., 2021).

E-mail address: zhzhihui@cugb.edu.cn (Z. Zhang).

^{*} Corresponding author.

The climate shifts have been linked to the atmospheric pCO_2 (Montañez et al., 2007; Montañez et al., 2016; Chen et al., 2018; Richey et al., 2020), tectonically paced rock weathering regimes (Goddéris et al., 2017; Yang et al., 2020), and volcanism (Yin et al., 2007; Korte et al., 2010; Korte and Kozur, 2010). Continental weathering trends have a discernable relationship to climate change, i.e., intensified chemical weathering corresponds to higher temperature and precipitation, while weakened weathering intensity to lower temperature and precipitation (Wang et al., 2020; Yang et al., 2020). Volcanism can discharge large volumes of CO_2 and CH_4 into the atmosphere, increasing atmospheric greenhouse gas concentration will result in global warming (Yin et al., 2007; Bond and Grasby, 2017), but the negative radiative forcing of volcanic sourced sulfate aerosols can also lead to global cooling (Soreghan et al., 2019; Lu et al., 2021).

Volcanic eruptions can release large amounts of Hg and cause enrichment of Hg in the Earth-surface system, which can easily overwhelm the background detrital Hg flux (Pyle and Mather, 2003; Zambardi et al., 2009). The residence time of Hg in the atmosphere has enough time (0.5 to 2 yrs) to ensure its wide dispersal after a major volcanic eruption (Selin, 2009; Driscoll et al., 2013). Mercury element derived from volcanism has the potential to be recorded in contemporaneous sedimentary rocks (Lu et al., 2021). Therefore, Hg concentrations have been extensively considered as an indicator of ancient volcanism (Nriagu and Becker, 2003; Pyle and Mather, 2003; Sial et al., 2013; Percival et al., 2015). For example, Lu et al. (2021) suggested that volcanism was an important driver for late Pennsylvanian to earliest Cisuralian shifts in global climates. Climate warming in southern North China at the Permo-Carboniferous transition likely tightly corresponds

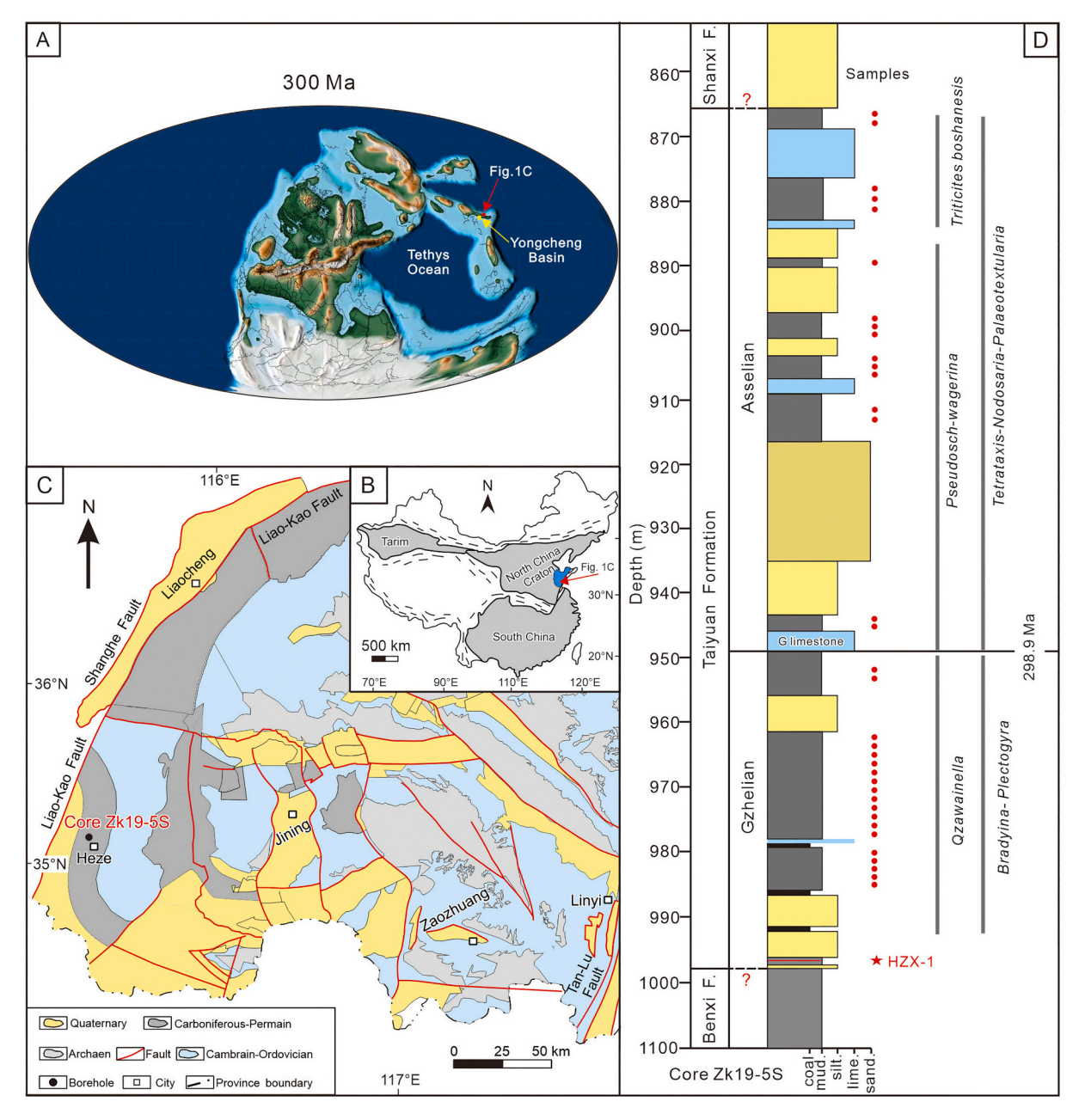


Fig. 1. Location and stratigraphic column for the study area. (A) \sim 300 Ma paleogeographic reconstruction from Scotese (2014) showing the positions of the studied area and the Yongcheng Basin (Yang et al., 2020). (B) Present location of the Western Shandong in North China Craton (NCC). (C) Regional geologic map of the Western Shandong showing the position of the core Zk19-5S. (D) Stratigraphic column of the core Zk19-5S with biological fossils (Zhang et al., 1989; Li et al., 2015). The red dots represent mudstone samples. The red five-pointed star represents the tuffaceous claystone sample. Benxi F. = Benxi Formation, Shanxi F. = Shanxi Formation. (For interpretation of the references to colour in this figure legend, the reader is referred to the web version of this article.)

with the LIP event in the Skagerrak center, which is correlated using high precision zircon U—Pb ages and weathering trends (Yang et al., 2020). However, this hypothesis lacks the record of mercury as valid evidence of volcanism.

In the present study, we investigate the Pennsylvanian to early Cisuralian Taiyuan Formation to show the relationships between volcanism and climate transitions. Focusing on the core Zk19-5S in the Western Shandong of the North China Craton (NCC), we report U—Pb zircon ages and derive a record of chemical weathering indices from a cored uppermost Carboniferous through the lower Permian succession. This study also analyzes mercury concentrations to identify intervals of volcanism and organic carbon isotope ($\rm S^{13}C_{org}$) values to evaluate perturbations in the global carbon cycle. Our data suggest that this climate warming event at the Permo-Carboniferous transition may correspond with the volcanism.

2. Geological setting

During the Permo-Carboniferous the NCC was surrounded by the Inner Mongolia uplift (IMU) to the north, the North Qinling Belt (NQB) to the south, warm waters of the Tethys Ocean to the west, and the Panthalassic Ocean to the east, was located in the northeastern margin of the Paleo-Tethys Ocean (PTO) (Fig. 1A), with a latitude of approximately 5–15°N (Embleton et al., 1996; Muttoni et al., 2003; Muttoni et al., 2009; Dong et al., 2011; Huang et al., 2018; Yuan and Yang, 2015; Dong and Santosh, 2016). The Western Shandong is located in the east of the NCC, bounded by the Tan-Lu fault zone in the east and the Liao-Kao fault in the west (Jin et al., 1999; Niu et al., 2004; Fig. 1B).

Fold structures and fault structures are widely distributed in the Western Shandong. The main fold structure is a monoclinal structure, and the stratigraphic strike is NE-SW and NW-trending (Fig. 1B). The eastern part of the Western Shandong is bounded by the Tan-Lu fault zone, which had a significant effect on tectonic magmatic activity and mineralization in the Western Shandong. The fault structures in the southern and central hills and mountains are well exposed, and the faults in the north and west are mostly covered by quaternary sediments (Jin et al., 1999). Core Zk19-5S was recovered from the Heze city of Shandong province in eastern North China (Fig. 1B). It is preserved in a dedicated core storage facility and is thus free of modern surface weathering, making it very convenient for examination. The stratigraphic succession and rock types in the target strata in the core Zk19-5S of the Heze city are shown in Fig. 1C. The Taiyuan Formation is a broadly coastal and shallow marine deposit of very similar aspects to the cyclothymic successions of North America and Europe (Wang, 1985; Lv et al., 2011; Davydov, 2014; Lv and Chen, 2014; Yang et al., 2020). The sedimentary lithology of the Taiyuan Formation is mainly successions of sandstones, siltstones, mudstones, and coal seams. It is separated from the Benxi Formation by a layer of gray, thick-bedded coarse-grained quartz sandstone, with the remainder of the Taiyuan Formation comprising mudstones, limestones, and sandstones deposited in a range of carbonate and detrital coastal depositional environments. It is also separated from the Shanxi Formation by a mudstone. The bottom of the Taiyuan Formation contains a thin layer of tuffaceous claystone (Fig. 1C).

3. Sampling and analytical methods

A total of 35 mudstone samples were collected from the Taiyuan Formation from core Zk19-5S. Vertical sampling locations are shown in Fig. 1C. The samples were crushed using an agate ball and sieved through a < 200 mesh and divided for total organic carbon (TOC) analysis, $\delta^{13}C_{org}$ analysis, major elements analysis, trace elemental analyses, and mercury concentration analysis. The major elements, trace elements, and TOC were detected in Tianjin Center, China Geological Survey, the $\delta^{13}C_{org}$ analysis, and mercury concentration analysis were detected in Beida Zhihui Microstructure Analysis and Testing Center Co.,

LTD. Samples for TOC were first treated with phosphoric acid to remove inorganic carbon, and then the TOC values were measured using a carbon-sulfur analyzer (CS580-A) with the lower detection limits of 100 mg/g and an absolute analysis error of $\pm 0.2\%$. $\delta^{13}C_{org}$ analysis was performed using a stable isotope mass spectrometer (MAT253), and $\delta^{13}C_{org}$ values are expressed in per mil (‰) with respect to the Vienna Pee Dee Belemnite (VPDB) standard, with the absolute analysis error of $\pm 0.1\%$. The X-ray fluorescence spectrometry (PW2404) with the relative analysis error of $\pm 5\%$ was used to determine the content of major-element oxides (SiO₂, A1₂O₃, CaO, K₂O, Na₂O, Fe₂O₃, MnO, MgO, TiO₂, and P₂O₅). The trace elements were determined using an Inductively-coupled plasma mass spectrometer (LA-ICPMS).

Mercury concentration was undertaken using a Lumex RA-915 \pm mercury analyzer with lower detection limits of 2 ng/g and a relative analysis error of \pm 5%. More details of the analytical method are described by Liao et al. (2016), Hu et al. (2019), and Chu et al. (2020). In this study, mercury enrichment anomalies have been used to indicate the presence of volcanic activity due to their relationship with volcanic eruptions and magmatic intrusions (Sanei et al., 2012; Grasby et al., 2013; Chen and Xu, 2019). At the same time, mudstones can retain information not only about the nature of the source material but also about its weathering history (Garver and Scott, 1995; Yang et al., 2020).

In order to establish an age model for the Permo-Carboniferous succession in the Western Shandong in NCC, the tuffaceous claystone sample (Fig. S1) from the Taiyuan Formation was obtained by using the zircon U—Pb dating method in this study. After crushing, grinding, sieving, and heavy liquid and magnetic separation, euhedral zircon crystals with clear oscillatory zoning under the cathodoluminescence (CL) microscope were selected for U—Pb zircon isotope analysis. Zircon grains were then analyzed for U, Th, and Pb isotopes by LA-ICPMS at Langfang Yuneng Rock Mineral Separation Technology Service. Data Cal and Isoplot 3.0 software were used for the age analysis, calculation, and the drawing of Concordia diagrams from the LA-ICPMS data. Zircon grains were then analyzed for Th, and Pb isotopes by LA-ICPMS at the Wuhan Shangpu Analysis Technology Co., Ltd. Further details of this technique are given by Lu et al. (2021).

4. Result

4.1. Zircon U-Pb dating

One tuffaceous claystone was sampled from the lowermost part of the Taiyuan Formation which is similar to other Late Paleozoic tuffs from the NCC (Yang et al., 2020; Lu et al., 2021). One hundred zircon crystals were separated from the sample in the core Zk19-5S from the NCC in the Western Shandong (HZX-1), with crystal sizes varying from 50 to 150 µm. Individual zircon crystals show euhedral morphology and clear oscillatory zoning in cathodoluminescence (CL) distinctive of magmatic zircon (Fig. 2A). Results of zircon U—Pb laser ablation inductively coupled plasma mass spectrometry (LA-ICPMS) dating are shown in Fig. 2 and Table S1. From sample HZX-1 a total of 78 concordant age values were determined with a bimodal age distribution (Fig. 2B); the younger peak has a weighted mean $^{206}\text{Pb}/^{238}\text{U}$ age of 301.3 \pm 1.1 Ma (MSWD = 1, n = 64), while the older peak has a weighted mean $^{206}\text{Pb}/^{238}\text{U}$ age of 437.5 \pm 2.8 Ma (MSWD = 0.83, n = 14)

We interpret the weighted mean ages from the younger peaks as the sedimentary ages of the tuffaceous claystone horizon for the following reasons. Firstly, sample HZX-1 yielded 64 concordant age values, which were distributed in a younger peak (Fig. 2). Secondly, during the Pennsylvanian frequent volcanic activity provides the possibility for the frequent inputs of tuffaceous and pyroclastic materials into the depositional basin, and the ages of the younger peaks are consistent with a Pennsylvanian age. Finally, the distribution of the younger peak weighted mean ages is consistent with the Permo-Carboniferous ages determined from biostratigraphy. These ages indicate that the lowest

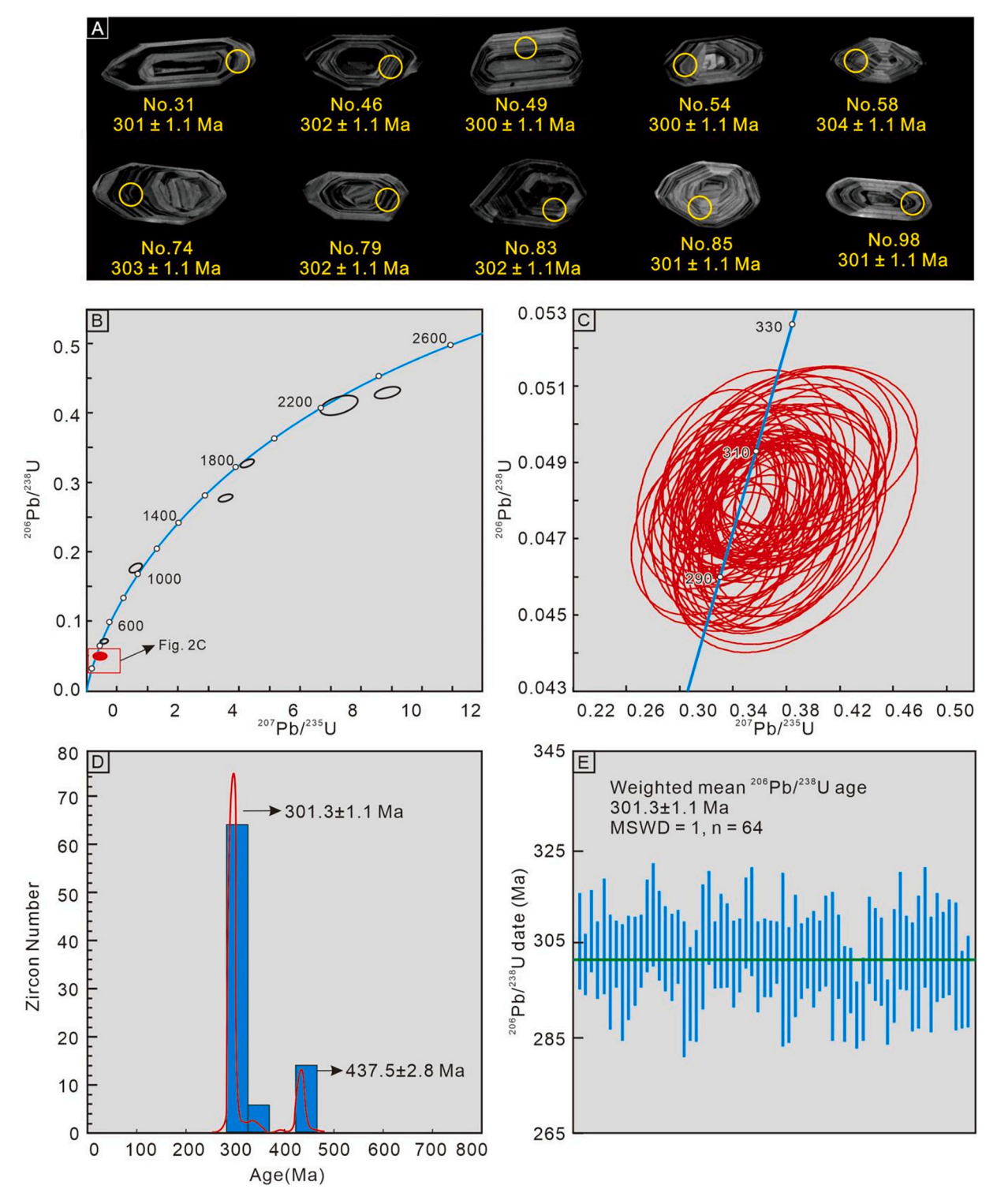


Fig. 2. Zircon U—Pb age distribution diagrams. (A) Typical zircon crystals of sample HZX-1 sample. (B—C) Zircon U—Pb of sample HZX-1 sample diagrams of sample HZX-1. (D) Zircon ²⁰⁶Pb/²³⁸U histogram of sample HZX-1. (E) The calculation of the weighted mean age of sample HZX-1.

Taiyuan Formation belongs to Middle Gzhelian.

4.2. Mudrock weathering index values and element indicators

Weathering indices of ancient detrital sediments can track changes in chemical weathering (Nesbitt and Young, 1982; Fedo et al., 1995; Scheffler et al., 2003; Rieu et al., 2007; Bahlburg and Dobrzinski, 2011; Yang et al., 2020). Various chemical weathering indices were used in

this study. We combine chemical index of alteration (CIA, Nesbitt and Young, 1982), weathering index of Parker (WIP, Parker, 1970), chemical index of weathering (CIW) (Harnois, 1988), chemical index of alteration without CaO (CIX, Dinis et al., 2017), plagioclase index of alteration (PIA, Fedo et al., 1995), and sodium depletion index (τ_{Na} , Rasmussen et al., 2011) to quantify the chemical weathering intensity experienced by the sources to the mudrocks. These indices involve different elements and thus can get rid of many sources of interference

and allow for evaluation of the potential influences exerted on sediment compositions. The major and trace elements are in Table S2 and Table S3, respectively. The detailed formulations and results for chemical weathering indices are listed in Table S4.

The geochemical weathering index values and element index values of Taiyuan Formation in Heze city core Zk19-5S are shown in Figs. 3 and 4, and all chemical weathering indices and element indexes are given in Table S4. CIA ranges from 77.9 to 92.4, with a mean of 85.7; WIP from 15.1 to 36.5, with a mean of 26.0; CIW ranges from 87.0 to 98.9, with a mean of 95.5; CIX from 81.7 to 93.0, with a mean of 87.0; PIA from 85.3 to 98.7, with a mean of 94.8; $\tau_{\rm Na}$ from -0.97 to -0.67, with a mean of -0.89. Sr/Ba from 0.14 to 4.45, with a mean of 1.48; Sr/Cu from 0.44 to 2.3, with a mean of 0.69; Rb/Sr from 0.05 to 0.63, with a mean of 0.29.

To simplify the discussion and interpretation of the results, we defined two intervals in the Heze city core Zk19-5S profile: VA-I (Upper part of Taiyuan Formation; \sim 910-900 m) and VA-II (Lower part of Taiyuan Formation; \sim 985-955 m), as indicated by the colored bands in Fig. 3. In VA-I, the chemical weathering indices of the CIA, CIX, CIW, PIA, Sr/Ba, and Sr/Cu have extremely high values, the WIP, τ_{Na} , and Rb/Sr are extremely low. In VA-II, the chemical weathering indices of the CIA, CIX, CIW, PIA, Sr/Ba, and Sr/Cu are in the high range, while the values of WIP, τ_{Na} , and Rb/Sr are in the low range.

4.3. TOC, mercury, and $\delta^{13}C_{\text{org}}$ values

Results for TOC and mercury are shown in Table S5 and Fig. 4. TOC values vary from 0.31%–5.61% (mean average = 2.11%). Hg concentrations vary from 2 ppb–205.00 ppb (mean average = 85.5 ppb). Mercury is generally hosted by organic matter, sulfide, and clay minerals in continental strata (Grasby et al., 2013, 2019; Racki et al., 2018; Shen et al., 2019a; Shen et al., 2019b). Organic matter is the major host of Hg according to the consistent changing trends of TOC and Hg (Fig. 4) (Grasby et al., 2013, 2019; Wang et al., 2018; Wang et al., 2019; Shen et al., 2019a; Shen et al., 2019b; Hammer et al., 2019). Therefore, Hg/TOC can discern enrichments independent of variations in TOC. Hg/

TOC ratios vary from 0.41 ppb/% to 448.4 ppb/% (mean average = 71.87 ppb/%). Results for $\delta^{13}C_{org}$ are shown in Table S5 and Fig. 4. $\delta^{13}C_{org}$ values vary from -22.4% to -28.2% (mean average = -23.96%). In this study, there is a negative isotope excursion during the early Asselian (named CIE-I).

At the same time, the episodes of Hg enrichment correspond to negative carbon isotope excursion. Thus, we determined the mercury peak values in the study area can be reliable proxies of volcanism. The peak of Hg enrichment corresponds to negative carbon isotope excursion of CIE-I. The negative carbon isotope excursions of CIE-I coincide with the mercury peak from which volcanism is likely to be a causal mechanism for the perturbations in the carbon cycle.

5. Discussion

5.1. Chronostratigraphy construction

The age of the Permo-Carboniferous strata in NCC is only broadly constrained based on biostratigraphy with enormous uncertainty (Zhu et al., 2005). However, the Carboniferous-Permian boundary has been well constrained by foraminifera in the Western Shandong (Zhang et al., 1989; Li et al., 2015). The paleontology in our core Zk19-5S is from Zhang et al. (1989) and Li et al. (2015), which provided a detailed paleontological analysis of the Taiyuan Formation in our studied area. Li et al. (2015) found that one marked limestone bed called "G limestone" in the middle of the Taiyuan Formation can be defined as the Carboniferous-Permian boundary in our studied area based on the biological fossils. The Carboniferous-Permian boundary is located at the bases of the *Pseudosch-Wagerina* and *Tetrataxis-Nodosaria-Palaeotextularia* assemblages, which were debuted at the bottom of the "G limestone" in the Taiyuan Formation in our studied area (Fig. 1D; Zhang et al., 1989; Li et al., 2015).

The sample HZX-1 was collected at the bottom of the Taiyuan Formation, with a weighted mean 206 Pb/ 238 U age of 301.3 \pm 1.1 Ma (Middle Gzhelian). Based on the ages of the sample HZX-1 and the

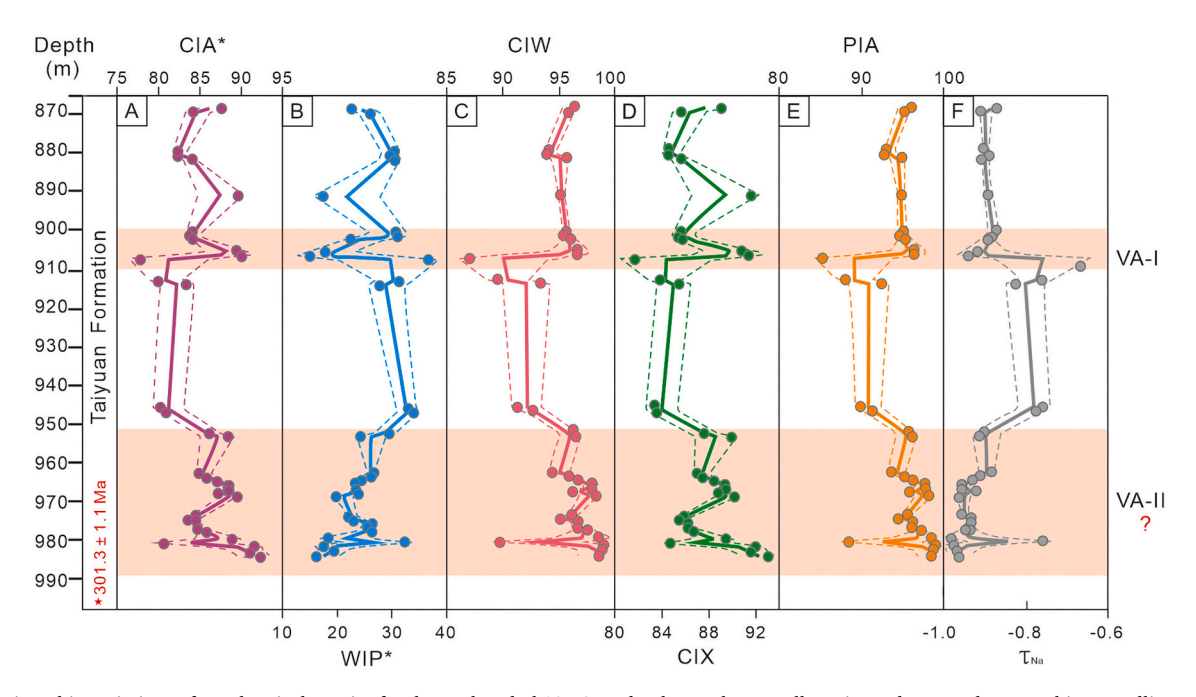


Fig. 3. Stratigraphic variations of geochemical proxies for the analyzed Zk19-5S mudrock samples. Locally estimated scatterplot smoothing trendlines using Acycle software (Li et al., 2019, 0.1 smoothing, solid lines) with 1σ bootstrapped errors (dashed lines) are shown for CIA*, CIW*, PIA, WIP, CIX, and τNa values (see the Table S4 for details). CIA = chemical index of alteration (Nesbitt and Young, 1982), WIP = Weathering index of Parker (Parker, 1970), CIW = Chemical index of weathering (Harnois, 1988), CIX = Chemical index of alteration without CaO (Dinis et al., 2017), PIA = Plagioclase index of alteration (Fedo et al., 1995), $τ_{Na}$ = Sodium depletion index (Rasmussen et al., 2011), CIA* = Corrected CIA, WIP* = Corrected WIP. The two pink bands indicate the potential warming events. (For interpretation of the references to colour in this figure legend, the reader is referred to the web version of this article.)

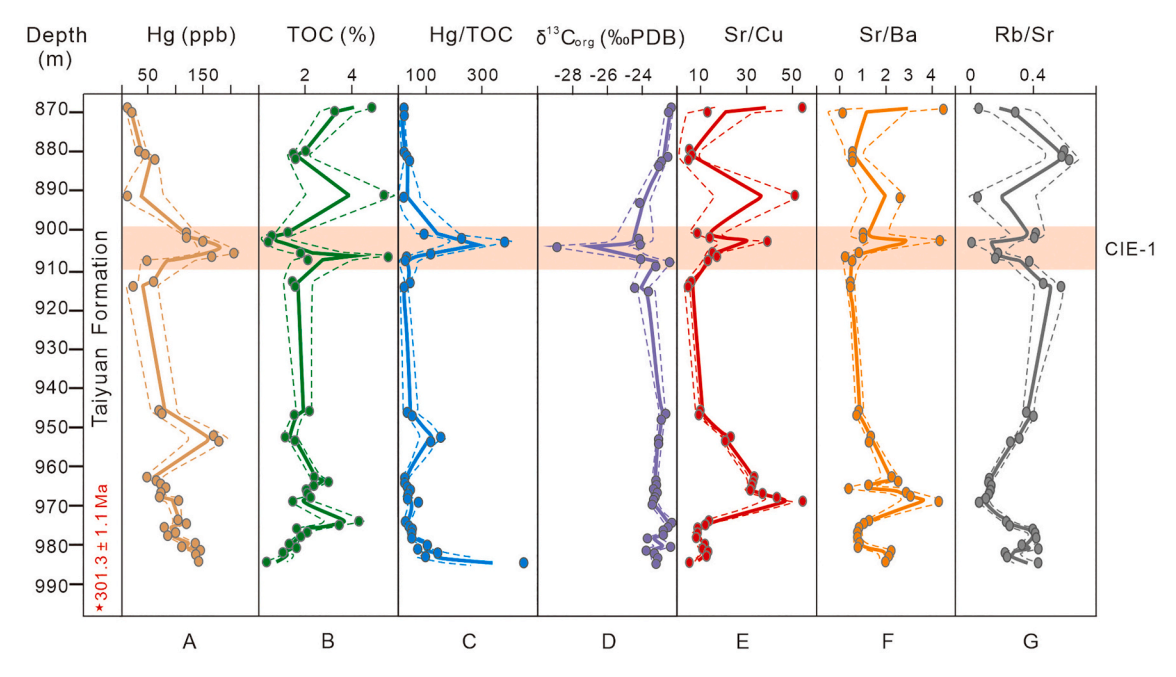


Fig. 4. Locally estimated scatterplot smoothing trendlines using Acycle software (Li et al., 2019, 0.1 smoothing, solid lines) with 1σ bootstrapped errors (dashed lines) are shown for Hg concentration, total organic carbon (TOC) values, Hg/TOC, organic carbon isotope ($\delta^{13}C_{org}$) values, Sr/Cu, Sr/Ba, and Rb/Sr in core Zk19-5S mudrock samples from the North China Craton. The pink band indicates a negative carbon isotope excursion. (For interpretation of the references to colour in this figure legend, the reader is referred to the web version of this article.)

Carboniferous-Permian boundary, an average depositional rate of 19.2 ± 1.1 m/Myr can be calculated for the Taiyuan Formation in our studied area. Similarly, Wu et al. (2021) and Lu et al. (2021) calculated the average depositional rate of the Taiyuan Formation in NCC at 19.1 m/Myr and $\cdot 25.6$ m/Myr based on the zircon U—Pb ages, respectively. This age model tightly constrains the Taiyuan Formation in our studied area to the middle Gzhelian-early Asselian (301.3 \pm 1.1 Ma - 296.2 ± 1.1 Ma). However, because the depositional rate could be variable in consideration of the difference in lithology, the proposed age model should have uncertainty. Despite this deficiency, a model age of $\sim\!295$ Ma acquired for the top of the Taiyuan Formation is consistent with a tuff zircon U—Pb age of 295.65 ± 0.08 Ma collected from the upper Taiyuan Formation in the Yongcheng Basin (Yang et al., 2020). Our zircon U—Pb age provides an age constraint for the Taiyuan Formation in the Western Shandong in NCC.

5.2. Weathering and paleotemperature trends

5.2.1. Eliminating the interference of non-weathering factors on weathering indices

Mudrocks have the potential to provide valuable weathering intensity information on their important source landscapes (Nesbitt and Young, 1982; Scheffler et al., 2003; Garzanti et al., 2013; Garzanti et al., 2014). Chemical weathering on continents is primarily controlled by temperature and moisture levels (Wronkiewicz and Condie, 1987; Johnsson and Basu, 1993; Sheldon, 2006; Sheldon and Tabor, 2009). Authigenic illite, montmorillonite chlorite, and carbonate minerals (calcite dolomite and siderite) have resulted in the change of chemical composition of the muddy sediments during diagenesis (Awwiller, 1993; Land et al., 1997; Lynch et al., 1997). For example, the potassium metasomatism of kaolinite often affects the mudstone composition during diagenesis (Awwiller, 1993; Fedo et al., 1995; Bloch, 1998; Rieu et al., 2007). The CIA is sensitive to potassium metasomatism and WIP is affected by sedimentary recycling and sorting-induced accumulation of quartz and zircon (Garzanti et al., 2013; Yang et al., 2020). Potassium metasomatism has no effect on the CIW (Gaillardet et al., 1999; Garzanti et al., 2013). Therefore, the Permo-Carboniferous climatic fluctuations of NCC can be revealed by chemical weathering indices without the interference of non-weathering factors or due to post-depositional metasomatism.

5.2.1.1. Diagenetic alteration. Some studies have shown that the dominant source for the early Permian sedimentary rocks in the Western Shandong corresponds with the composition of the upper continental crust of the interior of the NCC (INC; Chen and Liu, 1997; Fang, 1994). In this study, most analyses plot along with the predicted weathering trend of the INC in the Al_2O_3 -CaO* + Na_2O - K_2O (A-CN-K; where CaO* represents CaO in the silicate fraction only) diagram (Fig. 5A; Fedo et al., 1995). Therefore, the provenance inference of the study area is valid and reasonable. A-CN-K diagram indicates the existence of potassium metasomatism in the diagenetic process, which is caused by the conversion of kaolin (residual weathering product) to illite by reaction with K^+ -bearing pore waters (Fedo et al., 1995). This K-enrichment results in samples plotting towards the K apex of the A-CN-K triangle, with lower CIA and higher WIP values.

Thus, a correction of the potassium metasomatism of some samples deviating from the weathering trend is significant. Corrections for K-metasomatism can obtain the original weathering trend of each data point. In this study, according to the method of Yang et al. (2018a, 2018b), CIA and WIP values were corrected by potassium metasomatism on the A-CN-K diagram (Fig. 5B). CIA* values after correction ranged from 77.9 to 92.4, with a mean of 85.7, while WIP* from 15.1 to 36.5, with a mean of 25.3. In the Western Shandong, most of these corrected CIA values are >80.0 (Table S4). Our CIA* and WIP* values minimized the diagenetic influence of potassium metasomatism on the CIA and WIP, which indicates that CIA* and WIP* can serve as a more reliable proxy than CIA and WIP for reconstructing the paleoclimate (Yang et al., 2018a, 2018b). Therefore, the uncorrected CIA and WIP were not considered in the following discussion.

5.2.1.2. Sedimentary recycling. Sedimentary recycling refers to the process of weathering, denudation, transport, and deposition of sediments after deposition or diagenesis (McLennan, 1993; Cox et al., 1995; Jian et al., 2013). Stable minerals such as quartz and zircon accumulate

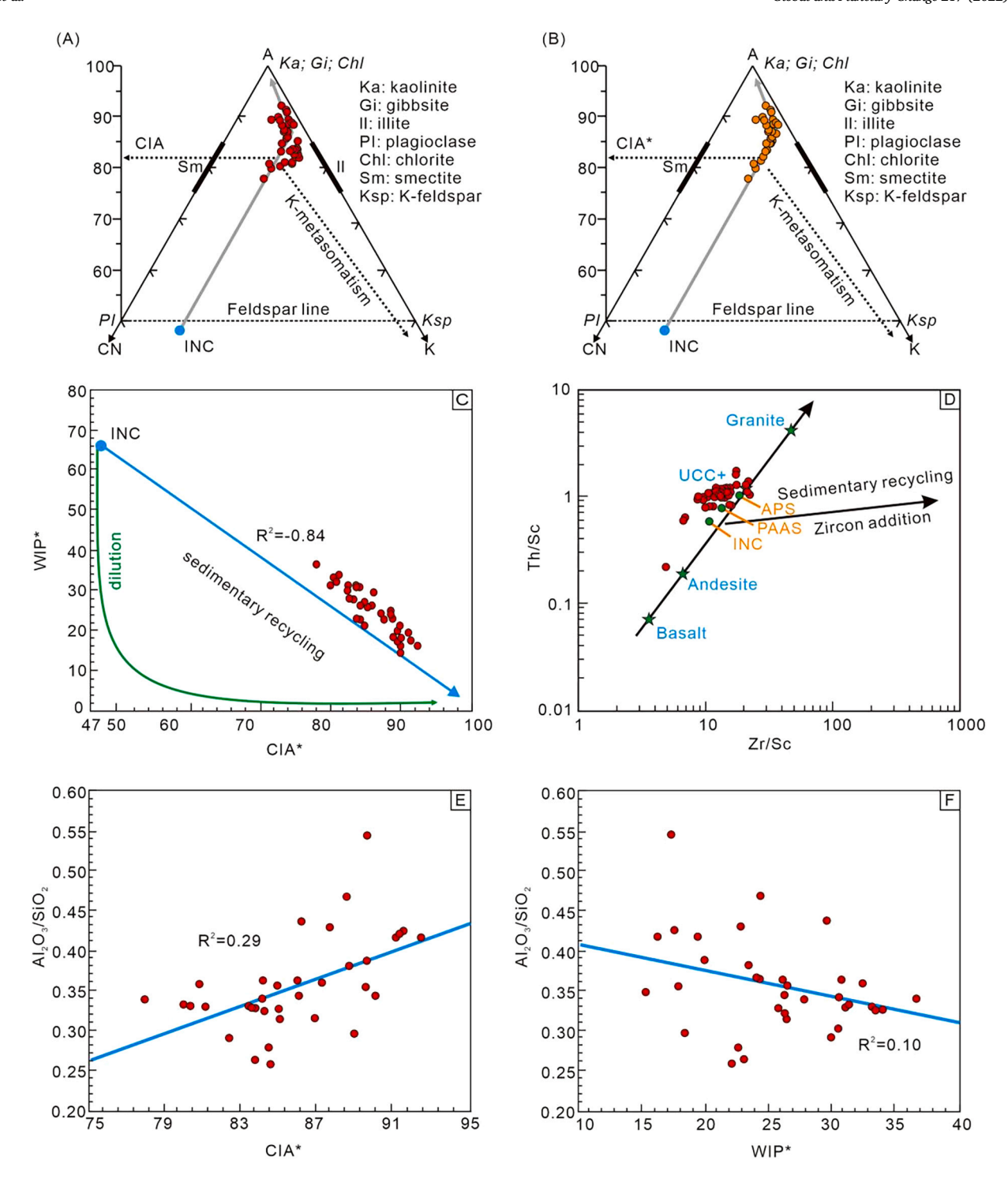


Fig. 5. Plots of analyzed mudstones. (A) Ternary diagrams of A-CN-K for core Zk19-5S mudrock samples from the North China Craton (NCC), based on the method described by Fedo et al. (1995). In the A-CN-K diagram, mudrock samples plot in the intermediate-intense weathering zones and generally mimic the ideal weathering trend of the upper continental crust of interior of the NCC (INC, Gao et al., 1998). (B) Corrected core Zk19-5S mudrock samples in Ternary diagrams of A-CN-K from the INC. $A = Al_2O_3$, $CN = CaO^* + Na_2O$, CIA = CACID = CACID

in the sediments during polycyclic reworking processes, thus diluting other components (McLennan, 1993; Cox et al., 1995; Armstrong-Altrin et al., 2004). Besides potassium metasomatism, it is another factor leading to the change in rock composition (Metcalfe et al., 2015). Therefore, this study attempts to exclude the effects of sedimentary recycling. As sedimentary recycling increases, the WIP (weathering index of Parker), which uses only the concentrations of Na, Mg, K, and Ca decreases linearly (Parker, 1970). The CIA, which uses concentrations of Al to calculate, is not affected by the process (Garzanti et al., 2013, 2014). CIA* was negatively correlated with WIP* in Taiyuan Formation in the Western Shandong ($R^2 = -0.84$), most samples showed a covariant relationship between CIA* and WIP* along with the projected INC weathering trend (Fig. 5C). It implies little effect from sedimentary recycling on the compositional trends.

Another additional proxy to evaluate possible recycling during deposition is the interaction diagram of Zr/Sc and Th/Sc (McLennan, 1993). The Zr/Sc ratio is low, meanwhile, the Th/Sc cross plot of the samples (Fig. 5D) has a good correspondence with the general trend determined by the parent rocks (Most samples are around UCC). It indicates that most components of the sedimentary rocks were not affected by recycling.

5.2.1.3. Hydraulic sorting. In addition to weathering, sorting is

particularly crucial for sedimentary rocks. Mineral sorting generally tends to increase the abundance of non-clay-clastic minerals with clay minerals as carriers (Sun et al., 2011; Singh and Rajamani, 2001; Roddaz et al., 2006). For example, as quartz and zircon minerals become enriched in the deposition of coarse-grained sediments, clay minerals are enriched in the residual finer-grained sediments during the sedimentation and sorting process (McLennan, 1993; Singh and Rajamani, 2001; Roddaz et al., 2006; Garzanti et al., 2013). The enrichment of quartz reduces the WIP value.

The Al_2O_3/SiO_2 ratio is widely applied as an indicator of hydraulic sorting and as a proxy for grain size (Bouchez et al., 2011; Yang et al., 2016). The Al_2O_3/SiO_2 ratios of all samples had a weak correlation with CIA* and WIP* (Fig. 5E; Fig. 5F). The lack of a correlation of the Al_2O_3/SiO_2 ratio with CIA* or WIP* implies that sedimentary sorting has a slight effect on the CIA* or WIP*.

5.2.1.4. Provenance interpretation. The state of element enrichment in sediments will change with the change of provenance, however, most immobile elements suffer minor losses during chemical weathering (Yang et al., 2016; Sun et al., 2022). The ratios between them are sensitive to the sedimentary provenance composition rather than to the chemical weathering intensity. For example, Th/Sc is a sensitive and simple index for identifying the overall source of terrigenous detritus

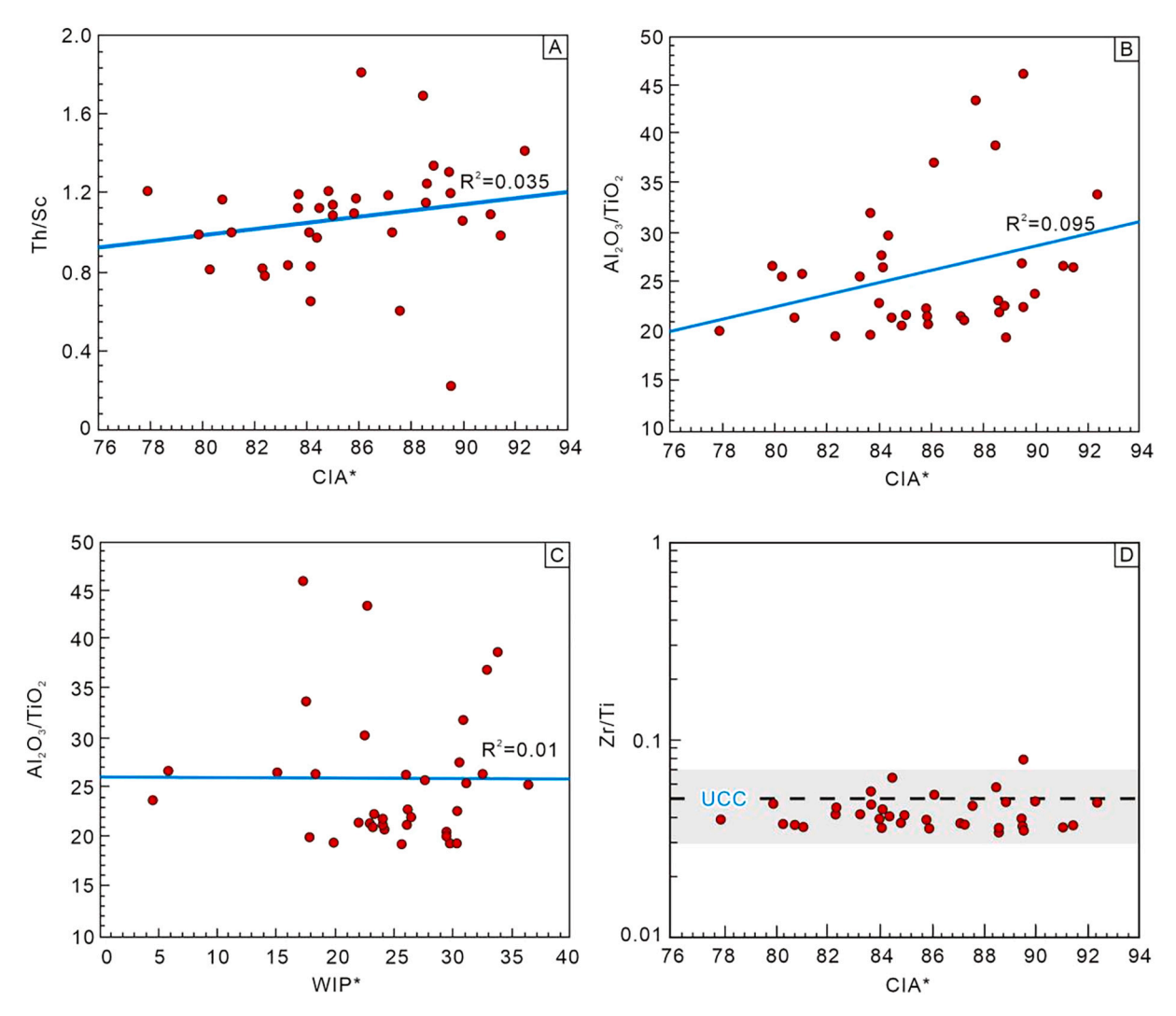


Fig. 6. (A) Cross plot of the CIA* with Th/Sc in the Taiyuan Formation mudstone sample set. CIA* = corrected chemical index of alteration. (B) Cross plot of the CIA* with Al_2O_3/TiO_2 in the Taiyuan Formation mudstone sample set. (C) Cross plot of the WIP* with Al_2O_3/TiO_2 in the Taiyuan Formation mudstone sample set. WIP* = corrected weathering index of Parker. (D) Cross plot of the CIA* with Zr/Ti in the Taiyuan Formation mudstone sample set.

because Th/Sc ratios vary >100 folds in detrital sediments with different provenances (Taylor and McLennan, 1985; McLennan, 1993; Cawood et al., 2003). There is no obvious correlation between CIA* and Th/Sc, indicating that the variations in CIA* were not affected by possible changes in provenance (Fig. 6A).

 Al_2O_3/TiO_2 ratio and Zr/Ti ratio are used to monitor the potential changes in source rock composition because they are controlled by source rock composition (Yang et al., 2018a, 2018b; Qi et al., 2020). Through the succession, CIA*, WIP* values have no explicit correlations with Al_2O_3/TiO_2 ratio ($R^2<0.10$), and this argues against weathering indices being influenced by sedimentary provenance (Fig. 6B; Fig. 6C). Zr/Ti ratio flattens close to the upper continental crust (UCC, Rudnick et al., 2003) and has no correlation with CIA*, which indicates the samples were unaffected by source composition (Fig. 6D).

5.2.2. Implications for Permo-Carboniferous paleoclimate and temperature changes

After eliminating the interference of non-weathering factors on weathering indices, the screened mudrock samples retain source chemical weathering signals. The sequential variations of CIA*, WIP*, CIW, CIX, PIA, and τ_{Na} values should accordingly reflect the chemical weathering trends of the source region (Nesbitt and Young, 1982; Johnsson and Basu, 1993; Scheffler et al., 2003; Garzanti et al., 2014).

These variations in chemical weathering trends reveal a remarkably consistent high peak in the upper part of Taiyuan Formation (early Asselian; ~298 Ma–297.5 Ma; numbered VA-I) and high values in the lower part of Taiyuan Formation (late Gzhelian; numbered VA-II) (Fig. 7A; Fig. 7B). The CIA* values of VA-II were relatively high, oscillating between 80.74 and 92.40. The CIA* in the upper part of Taiyuan Formation (early Asselian; VA-I) reveals a remarkable increase, followed by an immediate decrease of similar magnitude in weathering intensity.

A peak value of CIA* occurred at the depth of 906.5 m (\sim 298 Ma), indicating that there was an obvious warming event (VA-I).

Reconstruction of paleoclimate and paleotemperature have utilized stable isotopes (Mii et al., 2001; Korte et al., 2005; Buggisch et al., 2008; Grossman et al., 2008; Korte and Kozur, 2010; Korte et al., 2010; Chen et al., 2018, 2022), Biological palynology (Cai et al., 2012; Miao et al., 2013; Davydov, 2014), organic geochemistry (Meyers, 1994; Meyers, 1997) and sea-level change (Isbell et al., 2003; Miller et al., 2005; Fielding et al., 2008; Haq and Schutter, 2008). Modern large-river estuary suspended-sediment analyses show CIA values changing with latitude and land surface temperature (Yang et al., 2014). Yang et al. (2014) derived an empirical relationship between CIA and temperature and obtained global continental weathering trends and temperatures across an Early Permian glacial to post-glacial transition. Therefore, we applied this relationship to estimate the Taiyuan Formation paleotemperature trends on the NCC (Fig. 7A; Fig. 7B). An estimated warming of \sim 7 °C (18 °C to 25 °C) occurred in the upper part of Taiyuan Formation (early Asselian; ~298 Ma - 297.5 Ma; numbered VA-I). An estimated temperature increase of approximately 6 °C (20 °C to 26 °C) occurred in the lower part of Taiyuan Formation (late Gzhelian; numbered VA-II) with indications of oscillations.

Yang et al. (2016) proposed that the dependence of land surface soil chemical weathering intensity on the air temperature can be described by a $\tau_{Na}\text{-MAT}$ (mean annual temperature) transfer function. However, the formula needs to fulfill the following preconditions: 1) Because the surface soil chemical weathering in arid regions (annual rainfall <400 mm/yr) is controlled by humidity, there is no correlation with land surface temperature. Thus, the formula needs to be performed with precipitation >400 mm/yr, but not >4000 mm/yr; 2) Physical erosion rate < 100 m/Myr; 3) The transport process is not affected by sedimentary recycling and diagenesis.

Many studies showed that the climate in the Western Shandong was

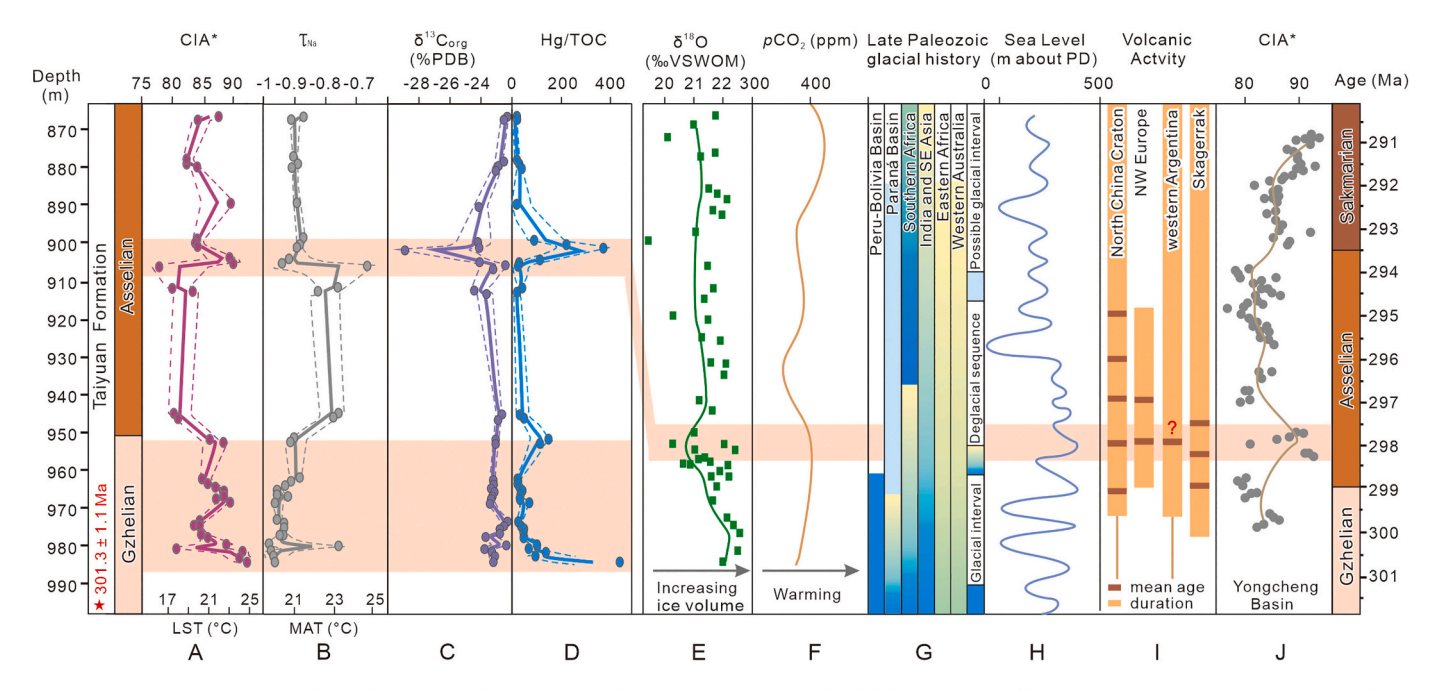


Fig. 7. Correlation of climate and weathering records of Permo-Carboniferous transition with global proxies. Locally estimated scatterplot smoothing trendlines using Acycle software (Li et al., 2019, 0.1 smoothing, solid lines) with 1σ bootstrapped errors (dashed lines) are shown for CIA*, τ_{Na} , and $\delta^{13}C_{org}$. (A) CIA* record and LST change in this study. CIA* = corrected chemical index of alteration (Fedo et al., 1995), LST = Land Surface Temperature (Yang et al., 2014). (B) τ_{Na} record and MAT change in this study. τ_{Na} = Sodium depletion index (Rasmussen et al., 2011), MAT = Mean Annual Temperature (Yang et al., 2016). (C) Organic carbon isotope ($\delta^{13}C_{org}$) variation in this study. (D) Hg/TOC ratios from the core Zk19-5S of the Western Shandong in the NCC. (E) Sequential variation of conodont oxygen isotope ($\delta^{18}C_{org}$) from the Naqing Section of South China (Chen et al., 2016). (F) Atmospheric partial pressure of CO₂ (pCO₂) from Montañez et al. (2007). (G) Sea level change from Haq and Schutter (2008). (H) Spatial and temporal distribution of the main record of the late Paleozoic deglaciation for Paraná Basin, Southern Africa, India, and SE Asia, Eastern Africa, and Western Australia (Rosa and Isbell, 2021; Isbell et al., 2021). (I) Timing of volcanic activity (Sato et al., 2015; Torsvik et al., 2008; Zhang et al., 2009). (J) The trend of CIA* values in Yongcheng Basin in NCC (Yang et al., 2020).

tropical-subtropical during the sedimentary period of the Taiyuan Formation (Chen et al., 2001a), with precipitation of about 1000–4300 mm/yr. North China had a wet coal-forming climate during the Early Permian (Fu et al., 2016), and the trend of weathering may not be controlled by rainfall supply. Therefore, the correlation between surface chemical weathering and the land surface temperature of the Taiyuan Formation in the Western Shandong was likely unaffected by rainfall. The estimated global average physical erosion rates range from 10 to 20 m/Myr in the early Permian (Wilkinson, 2005). For the source region of our studied formation, the physical erosion rate could be relatively stable because no evidence of dramatic changes in tectonic uplift around the Western Shandong during the early Permian. It applies to the second condition. We also discussed the weak effect of sedimentary recycling and diagenesis on the compositional trends.

It is indicated that the $\tau_{Na}\text{-MAT}$ transformation equation can be used to calculate the land surface paleotemperature of the Taiyuan Formation in the Western Shandong. Using the interior of the NCC as an average source composition (Gao et al., 1998), the τ_{Na} of Taiyuan Formation samples in the Western Shandong ranges from -0.67 to -0.97, with an average of -0.89, which transforms to a MAT of 15.3 °C–22.8 °C, with an average of 20.7 °C. And a warming of $\sim\!7$ °C (15 °C to 22 °C) occurred in the upper part of Taiyuan Formation (early Asselian; numbered VA-I). A temperature increase of approximately $\sim\!5.5$ °C (17.5 °C to 23 °C) occurred in the lower part of Taiyuan Formation (late Gzhelian; numbered VA-II) with indications of oscillations.

5.3. Implication for an early Asselian climate warming

A record of source weathering trends for the end-Carboniferous to early Permian in the Western Shandong in NCC provides evidence for an oscillating warm period (VA-II) during the Gzhelian and a significant warming event (VA-I) during the early Asselian. Yang et al. (2020) previously identified a warming event in the Yongcheng Basin equivalent to the VA-I event. However, Lu et al. (2021) did not find this warming event in the Liujiang Basin which is in the northeast of NCC. In this study, the zircon dating and sedimentation rate restricted the age of the warming event to approximately 298 Ma. The warming events in Yongcheng Basin were limited to about 298 Ma (Yang et al., 2020; Fig. 7J). Therefore, we conclude that the two warming events are the same event. In our study, a relatively warm event may have already been initiated in the late Gzhelian (VA-II; Fig. 6). The slight enrichment of Hg at \sim 955 m and \sim 985 m (VA-II) may be related to local and small-scale volcanic eruptions near our studied area, which have not caused recordable changes in paleoclimate as shown by CIA and $\delta^{13}C_{org}$ data. There is no more definitive evidence for this warming event, so VA-II will not be discussed in this study.

Modern surface soils in a supply-limited weathering regime tend to be chemically depleted to an extent (weathering intensity) largely controlled by precipitation and temperature (Riebe et al., 2004; Ferrier et al., 2016; Yang et al., 2020). Because there was a stable wet coalforming climate in NCC during the early Permian (Tabor and Poulsen, 2008; Montañez and Poulsen, 2013; Yang et al., 2020), we can reconstruct land surface temperature from CIA and τ_{Na} . Using the CIA and τ_{Na} based transfer function (Yang et al., 2014; Yang et al., 2016), a reconstructed land surface temperature trend through the sampled succession suggests distinct warming of $\sim\!\!7^\circ\text{C}$ in the early Asselian, immediately followed by rapid cooling (Fig. 7A; Fig. 7B).

Coincidently, there is a short-term rise in sea level in the earliest Asselian (Fig. 7H; Haq and Schutter, 2008). Moreover, conodont oxygen isotope (δ^{18} O) values from South China suggest a \sim 1% increase and a subsequent decrease in the earliest Asselian (Fig. 7E; Chen et al., 2016), it showed a consistent pattern for the tropical sea water temperature change. In the record of global CO₂, a peak in CO₂ still corresponds to the warming event in the Asselian (Fig. 7F; Montañez et al., 2007). Therefore, we received the same result as that of the conclusion of Yang et al. (2020).

The warming event in the early Asselian is also correlated with a spatial and temporal distribution of the main record of the late Paleozoic deglaciation and thus reflects significant deglaciation records in Paraná Basin, Southern Africa, India, and SE Asia, Eastern Africa, and Western Australia (Isbell et al., 2021; Rosa and Isbell, 2021). Although glaciation may have continued in the central and northern parts of the Paraná Basin, Antarctica, and Eastern Australia around 298 Ma (Isbell et al., 2008; Frank et al., 2015; Mottin et al., 2018), many sites show reduced glaciation at that time. A coincidence of deglaciation, increased CO₂ content, higher temperature and sea-level high stand likely defined a climate warm interval in the Asselian, which existed in the late Paleozoic maximum icehouse (Fig. 7).

In modern sediments, some sensitive element indicators are successfully applied to reconstruct paleoclimate (Gan et al., 2018; Mathews et al., 2020). The elements Sr, Cu, Ba, and Rb ratios are often used to analyze the paleoclimate characteristics (Lerman et al., 1995). Ratios of Sr/Ba indicate paleosalinity are used to investigate the paleoenvironment, while the ratios of Rb/Sr and Sr/Cu indicate paleoclimate. Sr/Cu ratio of 1.3-5.0 indicates warm and humid climate, and over 5.0 reflects drought conditions (Lerman et al., 1995). High Sr/Ba value represents high salinity, while low Sr/Ba value represents low salinity (Deng and Oian, 1993). High Rb/Sr value represents warm and humid climate, while low Rb/Sr value represents arid climate (Chen et al., 2001b). The increase of CIA indicates warmer and wetter climates (Nesbitt and Young, 1982). Therefore, normally the trends of Sr/Ba and Sr/Cu are opposite to CIA, while the trend of Rb/Sr is consistent with CIA. However, the results of the three elements proxies of samples from the Western Shandong are contrary to the expected conclusion (Fig. 4F; G; H). Perhaps the unnormal phoneme is affected by the paleogeographical environment in NCC, as high enrichment of Sr can not only be formed by concentrated deposition of lake water in arid and hot climates but also may be caused by transgression in warm and humid climates (Wang et al., 2009).

The transgressive events occurred in the late Paleozoic epicontinental basin of NCC (Li and Shan, 2000; Lv et al., 2011; Lv and Chen, 2014). In this study, we have analyzed sedimentary environments of samples from the Western Shandong by elements proxies. The relative contents of S, Ga, and Rb will change regularly from freshwater to seawater with different sedimentary environments (Degens et al., 1957; Zhang et al., 2021). Our sample reflects that the environment of the Western Shandong reached the salinity of the marine environment during the Late Paleozoic (Fig. 8A). B/Ga ratio of low 3.3 indicates continental facies, and over 4.4 reflects marine environment (Degens et al., 1957). And other sedimentologists also found Taiyuan Formation in the Western Shandong was in an epicontinental sea environment (Li and Shan, 2000; Lv and Chen, 2014; Lv et al., 2021). In this study, we arrived at this conclusion from the geochemistry characteristics (Fig. 8B). However, the B/Ga index needs to be combined with the geological background, as the inland saline lake environment is also characterized by high B/Ga (Zhang et al., 2021). Thus, combined with the changing trend of the CIA*, it can be determined that the Western Shandong is an epicontinental marine environment. The trend of Sr/Ba, Sr/Cu, and Rb/Sr are abnormal due to transgression, which is controlled by the sea level rose.

In the VA-I period (Early Asselian), the sea level rose due to the influence of climate warming, which led to increases of Sr/Cu and Sr/Ba values due to the influence of transgression in the Western Shandong. The shifts in $\delta^{18}{\rm O}$ and $\delta^{13}{\rm C}_{\rm org}$, atmospheric $p{\rm CO}_2$, sea-level variations, distribution of the main record of the late Paleozoic deglaciation, and CIA of the Yongcheng Basin confirmed a climate warm interval during the early Asselian.

5.4. Volcanism and $\delta^{13} C_{\text{org}}$ values linked to atmospheric pCO2 and paleoclimate

Mercury concentration has developed as a reliable proxy for the

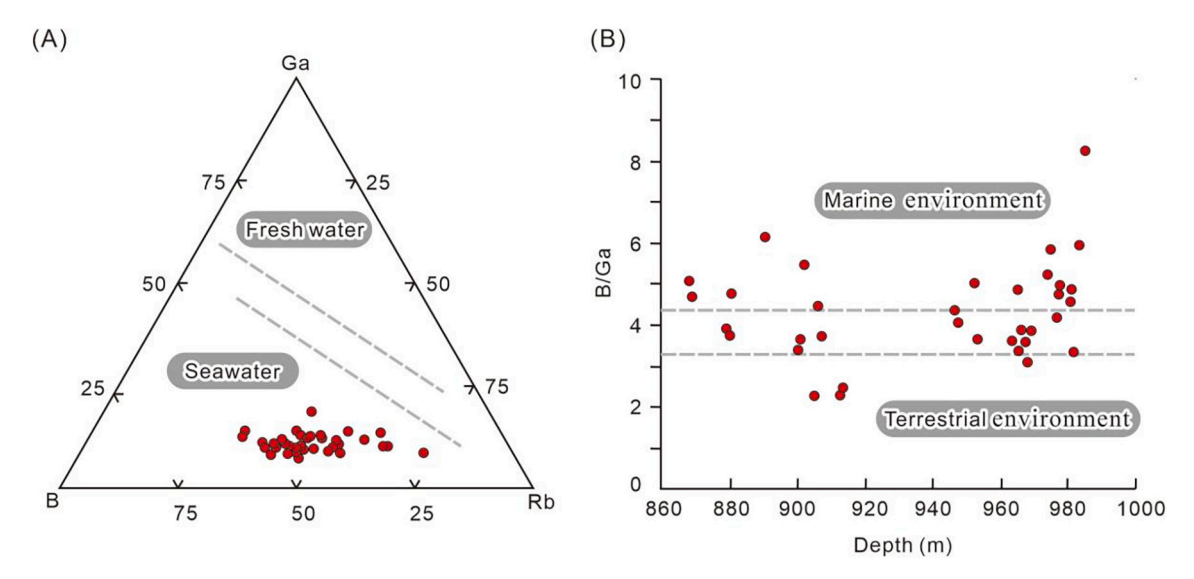


Fig. 8. Graphical analysis of the sedimentary environment. (A) Ternary diagrams of Ga-B-Rb for core Zk19-5S mudrock samples from the North China Craton (NCC), based on the method described by Yan et al. (1979). (B) Distributing disciplinarian of B/Ga in core Zk19-5S mudrock samples from the NCC (Degens et al., 1957).

evaluation of ancient volcanic fluxes (Grasby et al., 2019; Shen et al., 2019a; Shen et al., 2019b; Zhao et al., 2022). Volcanic emissions of Hg easily overwhelm the background detrital Hg during ancient large volcanic events (Pyle and Mather, 2003). The residence time of Hg in the atmosphere is long enough (0.5 to 2 yrs.; Selin, 2009) to be widely dispersed after major volcanism. Mercury in sediment can be adsorbed and removed quickly by organic matter and/or other minerals once deposited on the ocean surface (Zhao et al., 2022). Therefore, Hg can be used as a high-resolution volcanic proxy.

The record of terrestrial organic carbon isotopes is an effective proxy of the composition of CO_2 in ancient atmospheres (Wang, 2010; Turner, 2018; Vervoort et al., 2019). The eruptions and intrusions of volcanism will release significant amounts of Hg and comparatively isotopically heavy CO_2 (Javoy et al., 1984; Javoy et al., 1986), resulting in increasing atmospheric pCO_2 and Hg enrichment (Grasby et al., 2019; Vervoort et al., 2019). Magma can intrude into organic-rich sediments and release massive volumes of 13 C-depleted CO_2 (-22%), CH_4 (-60%), and large amounts of Hg (Grasby et al., 2019; Vervoort et al., 2019; Lu et al., 2021). It would cause an increase of Hg enrichment and atmospheric pCO_2 , with decreasing δ^{13} C values in the atmosphere (McElwain et al., 2005; Hesselbo et al., 2007).

The volcanic intensity curve inferred from the Hg/TOC ratios is shown in Fig. 7D and includes a significant peak in volcanic activity, intervals of obvious volcanic activity during the early Asselian (Fig. 7D; Fig. 7I). Subsequent rapid warming (\sim 298 Ma) in the earliest Asselian is indicated by the weathering trends in NCC and the $\delta^{18}O$ data from South China (Fig. 7E). This warm event is associated with a rapid increase of atmospheric pCO2 (Montañez et al., 2007) and a rise in short-term sea level (Haq and Schutter, 2008; Fig. 7H). Contemporaneous with coeval volcanism peak CIE-I in the study area (Fig. 7D), increases in atmospheric pCO2 values (Fig. 7F; Montañez et al., 2007) show that the increased atmospheric pCO2 and climate warming during the early Asselian. In the study area, a peak in volcanic activity corresponds to the negative excursion of $\delta^{13} C_{\text{org}}$ (CIE-I), suggesting a common source in heating organic-rich sediments by magma intrusion (Shen et al., 2019a; Shen et al., 2019b). All of these indicate that the early Asselian warming is probably related to volcanism.

During the Pennsylvanian, volcanism was globally widespread. The worldwide climate warming event at the Permo-Carboniferous transition may correspond with the volcanism in the Skagerrak-Centered Large Igneous Province (LIP), northwest Europe, western Argentina (pre-Choiyoi magmatism), or northern margin of the NCC (Sato et al., 2015; Torsvik et al., 2008; Zhang et al., 2009; Fig. 7I). Although the

uncertainties on these compiled ages for these volcanic activities are larger, which need to be improved in the future. As a consequence of an imprecise timescale of these volcanic eruptions, the peak of Hg in this study is only a sudden trend, which may also indicate that Hg is the result of regional volcanic activities in North China Craton, or volcanic activities had not been recorded in such a short period. However, compared with other climate indicators around the world at the same time range (CIA, δ^{13} Corg, δ^{18} O, TOC, ρ CO₂, and sea-level variations), it is more likely to be a global volcanic activity caused warming event.

In conclusion, the above volcanisms may extend from the Late Carboniferous to the early Permian (Sato et al., 2015; Torsvik et al., 2008; Zhang et al., 2009). The LIP event with the CO₂ outgassing may have resulted in an increased release of voluminous CO2 into the atmosphere, leading to a rapid rise in atmospheric pCO2. Yang et al. (2020) estimated that the magma at the Skagerrak-Centered LIP may have released 1.4×10^3 Pg CO₂ by using a conservative volume estimate of $\sim 1.5 \times 10^5 \text{ km}^3$ for the erupted basalts in Skagerrak-Centered LIP (Neumann et al., 2004; Torsvik et al., 2008) and scaling based on data estimated for the Deccan basalts (Self et al., 2006). Obviously, this is only a rough estimate. It is difficult to quantify the amount of CO₂ emitted without knowing crucial information like the original volume, eruptive rate, and magmatic process of the LIP (Yang et al., 2020). The early Asselian warming event may be driven by several of the volcanic activities mentioned above, or unrecorded volcanic activity for a short period of time. Due to the lack of an accurate age constrain of volcanic eruption, it is difficult to confirm the certain volcanic activity, which needs to be refined in future study.

However, the atmospheric pCO_2 during the Permo-Carboniferous transition is relatively low (Montañez et al., 2007; Montañez et al., 2016) and would be sensitive to the change of magmatic CO_2 input (Yang et al., 2020). At the same time, the change of the Hg also confirmed the existence of volcanic activity during the warming event. Taken together, the release of CO_2 from volcanic events was a critical driver of climate warming in the early Asselian.

An immediately cooling after the early Asselian warming (\sim 298 Ma-297.5 Ma) is indicated by the weathering trends in NCC (Fig. 7). It may have been the result of rapid post-eruptional weathering of the recently formed basaltic rocks in the Skagerrak-Centered LIP, which would drive the indicated atmospheric CO₂ drawdown and promoted a return to cooler icehouse conditions (Yang et al., 2020; Lu et al., 2021).

6. Conclusion

- 1) One tuffaceous claystone horizon was dated using zircon U—Pb method, yielding ages of 301.3 ± 1.1 Ma. The new dates allow for a boundary of the Carboniferous-Permian for the target strata in the Taiyuan Formation from the Western Shandong to be developed. This age model combined with biostratigraphy tightly constrains the studied succession of the Taiyuan Formation within the late Gzhelian-Asselian (301.3 ± 1.1 Ma 296.2 ± 1.1 Ma).
- 2) The trends in multiple chemical weathering indices are calculated from the geochemical composition of mudstones within the Taiyuan Formation to demonstrate climatic change in the West Shandong of NCC during the Permo-Carboniferous. The potential effects of provenance change, diagenesis, sedimentary recycling, and hydraulic sorting were excluded by using the specific chemical ratios through the interval. The published empirical relationship of the corrected chemical index of alteration (CIA*) and τ_{Na} with the temperature of the source region indicates the rapid onset of warming in the middle-upper part of the Taiyuan Formation, which is dated as early Asselian. The high-temperature interval is consistent with the warm events in Yongcheng Basin in southern NCC.
- 3) The initiation of the high-temperature event during the middle-upper Asselian was accompanied by the occurrence of major warm events. The trends coincide with temperature changes, shifts in δ^{18} O, atmospheric pCO $_2$, sea-level variations, distribution of the main record of the late Paleozoic deglaciation, and CIA of the Yongcheng Basin, which suggest the earliest Permian climate perturbation with a temperature maximum at \sim 298 Ma.
- 4) Hg/TOC ratios vary from 0.41 ppb/% to 448.3 ppb/% and include one obvious peak (VA-I) that recorded increased volcanic intensity during the early Asselian. $\delta^{13}C_{org}$ values vary from -22.4% to -28.2% (mean average =-23.96%) and present a negative excursion. Hg/TOC ratios peaks of volcanic intensity VA-I coincide with the negative carbon isotope excursions (CIE-I) and also intervals of high atmospheric pCO_2 and the relatively high sea level. The study indicates that volcanism is a causal mechanism for increasing atmospheric pCO_2 and driving the global climate cycles through greenhouse gas emissions in the Paleozoic.

Declaration of Competing Interest

The authors declare that they have no known competing financial interests or personal relationships that could have appeared to influence the work reported in this paper.

Data availability

Data will be made available on request.

Acknowledgments

This work was financially supported by the National Natural Science Foundation of China (Grant No. 41972170) and the SDUST Research Fund (Grant No.2018TDJH101).

Appendix A. Supplementary data

Supplementary data to this article can be found online at https://doi.org/10.1016/j.gloplacha.2022.103934.

References

Armstrong-Altrin, J., Lee, Y.I., Verma, S.P., Ramasamy, S., 2004. Geochemistry of sandstones from the Upper Miocene Kudankulam Formation, southern India: implications for provenance, weathering, and tectonic setting. J. Sediment. Res. 74, 285–297.

- Awwiller, D., 1993. Illite/smectite formation and potassium mass transfer during burial diagenesis of mudrocks; a study from the Texas Gulf Coast Paleocene-Eocene. J. Sediment. Res. 63, 501–512.
- Bahlburg, H., Dobrzinski, N., 2011. A review of the Chemical Index of Alteration (CIA) and its application to the study of Neoproterozoic glacial deposits and climate transitions. Geol. Soc. Lond. Mem. 36, 81–92.
- Bloch, R., 1998. Additions of organometallic reagents to C= N bonds: reactivity and selectivity. Chem. Rev. 98, 1407–1438.
- Bond, D.P., Grasby, S.E., 2017. On the causes of mass extinctions. Palaeogeogr Palaeoclimatol. Palaeoecol. 478, 3–29.
- Bouchez, J., Gaillardet, J., France-Lanord, C., Maurice, L., Dutra-Maia, P., 2011. Grain size control of river suspended sediment geochemistry: Clues from Amazon River depth profiles. Geochem. Geophys. Geosyst. 12.
- Buggisch, W., Joachimski, M.M., Sevastopulo, G., Morrow, J.R., 2008. Mississippian $\delta^{13}C_{carb}$ and conodont apatite $\delta^{18}O$ records—their relation to the Late Palaeozoic Glaciation. Palaeogeogr. Palaeoclimatol. Palaeoecol. 268, 273–292.
- Cai, M., Fang, X., Wu, F., Miao, Y., Appel, E., 2012. Pliocene–Pleistocene stepwise drying of Central Asia: evidence from paleomagnetism and sporopollen record of the deep borehole SG-3 in the western Qaidam Basin, NE Tibetan Plateau. Glob. Planet. Chang, 94, 72–81.
- Cawood, P.A., Nemchin, A.A., Freeman, M., Sircombe, K., 2003. Linking source and sedimentary basin: Detrital zircon record of sediment flux along a modern river system and implications for provenance studies. Earth Planet. Sci. Lett. 210, 259–268.
- Chen, S., Liu, H., 1997. Carboniferous-Permian lithofacies and paleogeography in the eastern part of the North China platform. Reg. Geol. China 2, 259–266 (in Chinese with English abstract).
- Chen, J., Xu, Y., 2019. Establishing the link between Permian volcanism and biodiversity changes: insights from geochemical proxies. Gondwana Res. 75, 68–96.
- Chen, X., Ruan, Y., Boucot, A.J., 2001a. Paleozoic Climate Evolution in China. Science Press.
- Chen, J., Wang, Y., Chen, Y., Liu, L., Ji, J., Lu, H., 2001b. Rb and Sr geochemical characterization of the Chinese loess and its implications for palaeomonsoon climate. Acta Geol. Sin. 75, 259–266 (in Chinese with English abstract).
- Chen, B., Joachimski, M.M., Shen, S., Lambert, L.L., Lai, X., Wang, X., Chen, J., Yuan, D., 2013. Permian ice volume and palaeoclimate history: oxygen isotope proxies revisited. Gondwana Res. 24, 77–89.
- Chen, B., Joachimski, M.M., Wang, X., Shen, S., Qi, Y., Qie, W., 2016. Ice volume and paleoclimate history of the Late Paleozoic Ice Age from conodont apatite oxygen isotopes from Naqing (Guizhou, China). Palaeogeogr. Palaeoclimatol. Palaeoecol. 448, 151–161.
- Chen, J., Montañez, I.P., Qi, Y., Shen, S., Wang, X., 2018. Strontium and carbon isotopic evidence for decoupling of *p*CO₂ from continental weathering at the apex of the late Paleozoic glaciation. Geology 46, 395–398.
- Chen, J., Montañez, I.P., Zhang, S., Isson, T.T., Macarewich, S.I., Planavsky, N.J., Zhang, F., Rauzi, S., Daviau, K., Yao, L., 2022. Marine anoxia linked to abrupt global warming during Earth's penultimate icehouse. Proc. Natl. Acad. Sci. 119, e2115231119
- Chu, D., Grasby, S.E., Song, H., Dal Corso, J., Wang, Y., Mather, T.A., Wu, Y., Song, H., Shu, W., Tong, J., 2020. Ecological disturbance in tropical peatlands prior to marine Permian-Triassic mass extinction. Geology 48, 288–292.
- Condie, K.C., 1993. Chemical composition and evolution of the upper continental crust: contrasting results from surface samples and shales. Chem. Geol. 104, 1–37.
- Cox, R., Lowe, D.R., Cullers, R., 1995. The influence of sediment recycling and basement composition on evolution of mudrock chemistry in the southwestern United States. Geochim. Cosmochim. Acta 59, 2919–2940.
- Davydov, V., 2014. Warm water benthic foraminifera document the Pennsylvanian–Permian warming and cooling events-the record from the Western Pangea tropical shelves. Palaeogeogr. Palaeoclimatol. Palaeoecol. 414, 284–295.
- Degens, E., Williams, E., Keith, M., 1957. Environmental studies of Carboniferous sediments part I: geochemical criteria for differentiating marine from fresh-water shales. AAPG Bull. 41, 2427–2455.
- Deng, H., Qian, K., 1993. Sedimentary Geochemistry and Environmental Analysis. Gansu Science Technology Press, Lanzhou, pp. 18–31.
- Dietrich, P., Griffis, N.P., Le Heron, D.P., Montañez, I.P., Kettler, C., Robin, C., Guillocheau, F., 2021. Fjord network in Namibia: A snapshot into the dynamics of the late Paleozoic glaciation. Geology 49, 1521–1526.
- Dinis, P., Garzanti, E., Vermeesch, P., Huvi, J., 2017. Climatic zonation and weathering control on sediment composition (Angola). Chem. Geol. 467, 110–121.
- Dong, Y., Santosh, M., 2016. Tectonic architecture and multiple orogeny of the Qinling Orogenic Belt, Central China. Gondwana Res. 29, 1–40.
- Dong, Y., Zhang, G., Neubauer, F., Liu, X., Genser, J., Hauzenberger, C., 2011. Tectonic evolution of the Qinling orogen, China: review and synthesis. J. Asian Earth Sci. 41, 213–237.
- Driscoll, C.T., Mason, R.P., Chan, H.M., Jacob, D.J., Pirrone, N., 2013. Mercury as a global pollutant: sources, pathways, and effects. Environ. Sci. Technol. 47, 4967–4983.
- Embleton, B.J., McElhinny, M.W., Ma, X., Zhang, Z., Xiang Li, Z., 1996. Permo-Triassic magnetostratigraphy in China: the type section near Taiyuan, Shanxi province, North China. Geophys. J. Int. 126, 382–388.
- Fang, S., 1994. Lithofacies and paleogeography of Permian period in the southeastern of North China Platform North China. J. Geol. Min. Res. 97-104 (in Chinese with English abstract).
- Fedo, C.M., Wayne Nesbitt, H., Young, G.M., 1995. Unraveling the effects of potassium metasomatism in sedimentary rocks and paleosols, with implications for paleoweathering conditions and provenance. Geology 23, 921–924.

- Ferrier, K.L., Riebe, C.S., Jesse Hahm, W., 2016. Testing for supply-limited and kinetic-limited chemical erosion in field measurements of regolith production and chemical depletion. Geochem. Geophys. Geosyst. 17, 2270–2285.
- Fielding, C.R., Frank, T.D., Birgenheier, L.P., Rygel, M.C., Jones, A.T., Roberts, J., 2008. Stratigraphic imprint of the Late Palaeozoic Ice Age in eastern Australia: a record of alternating glacial and nonglacial climate regime. J. Geol. Soc. 165, 129–140.
- Frank, T.D., Shultis, A.I., Fielding, C.R., 2015. Acme and demise of the late Palaeozoic ice age: A view from the southeastern margin of Gondwana. Palaeogeogr. Palaeoclimatol. Palaeoecol. 418, 176–192.
- Fu, B., Liu, G., Liu, Y., Cheng, S., Qi, C., Sun, R., 2016. Coal quality characterization and its relationship with geological process of the Early Permian Huainan coal deposits, southern North China. J. Geochem. Explor. 166, 33–44.
- Gaillardet, J., Dupré, B., Allègre, C., 1999. Geochemistry of large river suspended sediments: silicate weathering or recycling tracer? Geochim. Cosmochim. Acta 63, 4037–4051
- Gan, H., Wang, H., Chen, J., Zhuang, X., Cao, H., Jiang, S., 2018. Geochemical characteristics of Jurassic coal and its paleoenvironmental implication in the eastern Junggar Basin, China. J. Geochem. Explor. 188, 73–86.
- Gao, S., Luo, T., Zhang, B., Zhang, H., Han, Y., Zhao, Z., Hu, Y., 1998. Chemical composition of the continental crust as revealed by studies in East China. Geochim. Cosmochim. Acta 62, 1959–1975.
- Garver, J.I., Scott, T.J., 1995. Trace elements in shale as indicators of crustal provenance and terrane accretion in the southern Canadian Cordillera. Geol. Soc. Am. Bull. 107, 440–453.
- Garzanti, E., Padoan, M., Setti, M., Najman, Y., Peruta, L., Villa, I.M., 2013. Weathering geochemistry and Sr-Nd fingerprints of equatorial upper Nile and Congo muds. Geochem. Geophys. Geosyst. 14, 292–316.
- Garzanti, E., Padoan, M., Setti, M., López-Galindo, A., Villa, I.M., 2014. Provenance versus weathering control on the composition of tropical river mud (southern Africa). Chem. Geol. 366, 61–74.
- Gastaldo, R.A., DiMichele, W.A., Pfefferkorn, H.W., 1996. Out of the Icehouse into the Greenhouse: A Late Paleozoic Analogue for Modern Global Vegetational Change. Gsa today
- Goddéris, Y., Donnadieu, Y., Carretier, S., Aretz, M., Dera, G., Macouin, M., Regard, V., 2017. Onset and ending of the late Palaeozoic ice age triggered by tectonically paced rock weathering. Nat. Geosci. 10, 382–386.
- Grasby, S.E., Sanei, H., Beauchamp, B., Chen, Z., 2013. Mercury deposition through the Permo-Triassic Biotic Crisis. Chem. Geol. 351, 209–216.
- Grasby, S.E., Them, T.R., Chen, Z., Yin, R., Ardakani, O.H., 2019. Mercury as a proxy for volcanic emissions in the geologic record. Earth Sci. Rev. 102880.
- Griffis, N.P., Montañez, I.P., Mundil, R., Richey, J., Isbell, J., Fedorchuk, N., Linol, B., Iannuzzi, R., Vesely, F., Mottin, T., 2019. Coupled stratigraphic and U-Pb zircon age constraints on the late Paleozoic icehouse-to-greenhouse turnover in south-central Gondwana. Geology 47, 1146–1150.
- Griffis, N., Mundil, R., Montanez, I., Richey, J., Dietrich, P., Le Heron, D., Kettler, C., Linol, B., Iannuzzi, R., 2021. Timing and potential Causes for the Demise of Earth's Penultimate Icehouse, GSA Connects 2021, pp. Paper No. 73-73.
- Grossman, E.L., Yancey, T.E., Jones, T.E., Bruckschen, P., Chuvashov, B., Mazzullo, S., Mii, H., 2008. Glaciation, aridification, and carbon sequestration in the Permo-Carboniferous: the isotopic record from low latitudes. Palaeogeogr. Palaeoclimatol. Palaeogeogl. 268, 222–233.
- Groves, J.R., Wang, Y., 2013. Timing and size selectivity of the Guadalupian (Middle Permian) fusulinoidean extinction. J. Paleontol. 87, 183–196.
- Groves, J.R., Yue, W., 2009. Foraminiferal diversification during the late Paleozoic ice age. Paleobiology 35, 367–392.
- Gulbranson, E.L., 2011. Paleoclimate Reconstruction of the Late Paleozoic Paganzo Group, Northwest Argentina. University of California, Davis.
- Hammer, Y., Jones, M.T., Schneebeli-Hermann, E., Hansen, B.B., Bucher, H., 2019. Are Early Triassic extinction events associated with mercury anomalies? A reassessment of the Smithian/Spathian boundary extinction. Earth Sci. Rev. 195, 179–190.
- Haq, B.U., Schutter, S.R., 2008. A chronology of Paleozoic sea-level changes. Science 322, 64–68.
- Harnois, L., 1988. The CIW index: a new chemical index of weathering. Sediment. Geol. 55, 319–322.
- Hesselbo, S.P., Jenkyns, H.C., Duarte, L.V., Oliveira, L.C., 2007. Carbon-isotope record of the Early Jurassic (Toarcian) Oceanic Anoxic Event from fossil wood and marine carbonate (Lusitanian Basin, Portugal). Earth Planet. Sci. Lett. 253, 455–470.
- Horton, D.E., Poulsen, C.J., Pollard, D., 2007. Orbital and CO2 forcing of late Paleozoic continental ice sheets. Geophys. Res. Lett. 34.
- Hu, F., Fu, X., Lin, L., Song, C., Tian, K., 2019. Marine Late Triassic-Jurassic carbonisotope excursion and biological extinction records: New evidence from the Qiangtang Basin, eastern Tethys. Glob. Planet. Chang. 185, 103093.
- Huang, B., Yan, Y., Piper, J.D., Zhang, D., Yi, Z., Yu, S., Zhou, T., 2018. Paleomagnetic constraints on the paleogeography of the East Asian blocks during Late Paleozoic and Early Mesozoic times. Earth-Sci. Rev. 186, 8–36.
- Isbell, J.L., Miller, M.F., Wolfe, K.L., Lenaker, P.A., Chan, M., Archer, A., 2003. Timing of late Paleozoic glaciation in Gondwana: Was glaciation responsible for the development of Northern Hemisphere cyclothems? Geol. Soc. Am. Spec. Pap. 5–24.
- Isbell, J.L., Koch, Z.J., Szablewski, G.M., Lenaker, P.A., Fielding, C., Frank, T., 2008.
 Permian glacigenic deposits in the Transantarctic Mountains, Antarctica. In:
 Resolving the late Paleozoic ice age in time and space: Geological Society of America Special Paper, 441, pp. 59–70.
- Isbell, J.L., Henry, L.C., Gulbranson, E.L., Limarino, C.O., Fraiser, M.L., Koch, Z.J., Ciccioli, P.L., Dineen, A.A., 2012. Glacial paradoxes during the late Paleozoic ice age: Evaluating the equilibrium line altitude as a control on glaciation. Gondwana Res. 22. 1–19.

- Isbell, J.L., Vesely, F.F., Rosa, E.L., Pauls, K.N., Fedorchuk, N.D., Ives, L.R., McNall, N.B., Litwin, S.A., Borucki, M.K., Malone, J.E., 2021. Evaluation of physical and chemical proxies used to interpret past glaciations with a focus on the late Paleozoic Ice Age. Earth Sci. Rev. 221, 103756.
- Isozaki, Y., Kawahata, H., Ota, A., 2007. A unique carbon isotope record across the Guadalupian–Lopingian (Middle-Upper Permian) boundary in mid-oceanic paleoatoll carbonates: the high-productivity "Kamura event" and its collapse in Panthalassa. Glob. Planet. Chang. 55, 21–38.
- Javoy, M., Pineau, F., Demaiffe, D., 1984. Nitrogen and carbon isotopic composition in the diamonds of Mbuji Mayi (Zaire). Earth Planet. Sci. Lett. 68, 399–412.
- Javoy, M., Pineau, F., Delorme, H., 1986. Carbon and nitrogen isotopes in the mantle. Chem. Geol. 57, 41–62.
- Jian, X., Guan, P., Zhang, W., Feng, F., 2013. Geochemistry of Mesozoic and Cenozoic sediments in the northern Qaidam basin, northeastern Tibetan Plateau: implications for provenance and weathering. Chem. Geol. 360, 74–88.
- Jin, Z., Liu, Z., Shi, Z., 1999. Distribution patterns and formation mechanism of fault structures in the Western Shandong province. J. China Univ. Petroeum 23, 1–5 (in Chinese with English abstarct).
- Johnsson, M.J., Basu, A., 1993. The system controlling the composition of clastic sediments. Spec. Paper Geol. Soc. Am. 284, 1–20.
- Korte, C., Kozur, H.W., 2010. Carbon-isotope stratigraphy across the Permian–Triassic boundary: a review. J. Asian Earth Sci. 39, 215–235.
- Korte, C., Jasper, T., Kozur, H.W., Veizer, J., 2005. δ¹⁸O and δ¹³C of Permian brachiopods: a record of seawater evolution and continental glaciation. Palaeogeogr. Palaeoclimatol. Palaeoecol. 224, 333–351.
- Korte, C., Pande, P., Kalia, P., Kozur, H.W., Joachimski, M.M., Oberhänsli, H., 2010. Massive volcanism at the Permian–Triassic boundary and its impact on the isotopic composition of the ocean and atmosphere. J. Asian Earth Sci. 37, 293–311.
- Land, L.S., Mack, L.E., Milliken, K.L., Leo Lynch, F., 1997. Burial diagenesis of argillaceous sediment, south Texas Gulf of Mexico sedimentary basin: a reexamination. Geol. Soc. Am. Bull. 109, 2–15.
- Le Heron, D.P., Kettler, C., Griffis, N.P., Dietrich, P., Montañez, I.P., Osleger, D.A., Hofmann, A., Douillet, G., Mundil, R., 2021. The Late Palaeozoic Ice Age unconformity in southern Namibia viewed as a patchwork mosaic. In: The Depositional Record.
- Lerman, A., Imboden, D.M., Gat, J.R., Chou, L., 1995. Physics and Chemistry of Lakes.
 Springer-Verlag Berlin.
- Li, Z., Shan, S., 2000. Characteristics of high-resolution sequences of coal bearing strata in epicontinental basin. Geol. Explor. 13–16 (in Chinese with English abstract).
- Li, S., Yuan, L., Yin, T., Zhao, X., Cui, X., 2015. The foraminiferal fauna of the Taiyuan Formation and the Carboniferous-Permian boundary in Zibo, Shandong Province. Geol. J. China Univ. 21, 196–202 (in Chinese with English abstract).
- Li, M., Hinnov, L., Kump, L., 2019. Acycle: time-series analysis software for paleoclimate research and education. Comput. Geosci. 127, 12–22.
- Liao, Z., Hu, W., Cao, J., Wang, X., Yao, S., Wan, Y., 2016. Permian–Triassic boundary (PTB) in the Lower Yangtze Region, southeastern China: A new discovery of deepwater archive based on organic carbon isotopic and U–Pb geochronological studies. Palaeogeogr. Palaeoclimatol. Palaeoecol. 451, 124–139.
- Lu, J., Wang, Y., Yang, M., Shao, L., Hilton, J., 2021. Records of volcanism and organic carbon isotopic composition (8¹³C_{org}) linked to changes in atmospheric pCO2 and climate during the Pennsylvanian icehouse interval. Chem. Geol. 570, 120168.
- Lv, D., Chen, J., 2014. Depositional environments and sequence stratigraphy of the Late Carboniferous— Early Permian coal-bearing successions (Shandong Province, China): Sequence development in an epicontinental basin. J. Asian Earth Sci. 79, 16–30.
- Lv, D., Li, Z., Wei, J., Liu, H., Ning, W., 2011. Sedimentary characteristics and geological significance of condensed section of neopaleozoic of western Shandong in North China. J. Southwest Petrol. Univ. Nat. Sci. Edition 33, 14–20 (in Chinese with Englsih abstract).
- Lv, D., Hu, G., Van Loon, A.J., Wu, D., 2021. Depositional environments of the Carboniferous-Permian Taiyuan Formation (southern North China Block) as deduced from trace elements and from carbon and oxygen isotopes. Geol. Quart. 65, 65-61.
- Lynch, F.L., Mack, L.E., Land, L.S., 1997. Burial diagenesis of illite/smectite in shales and the origins of authigenic quartz and secondary porosity in sandstones. Geochim. Cosmochim. Acta 61, 1995–2006.
- Mathews, R.P., Pillai, S.S.K., Manoj, M., Agrawal, S., 2020. Palaeoenvironmental reconstruction and evidence of marine influence in Permian coal-bearing sequence from Lalmatia Coal mine (Rajmahal Basin), Jharkhand, India: a multi-proxy approach. Int. J. Coal Geol. 224, 103485.
- McElwain, J.C., Wade-Murphy, J., Hesselbo, S.P., 2005. Changes in carbon dioxide during an oceanic anoxic event linked to intrusion into Gondwana coals. Nature 435, 479–482
- McLennan, S.M., 1993. Weathering and global denudation. J. Geol. 101, 295–303.
 Metcalfe, I., Crowley, J., Nicoll, R., Schmitz, M., 2015. High-precision U-Pb CA-TIMS calibration of Middle Permian to Lower Triassic sequences, mass extinction and extreme climate-change in eastern Australian Gondwana. Gondwana Res. 28, 61–81.
- Meyers, P.A., 1994. Preservation of elemental and isotopic source identification of sedimentary organic matter. Chem. Geol. 114, 289–302.
- Meyers, P.A., 1997. Organic geochemical proxies of paleoceanographic, paleolimnologic, and paleoclimatic processes. Org. Geochem. 27, 213–250.
- Miao, Y., Fang, X., Wu, F., Cai, M., Song, C., Meng, Q., Xu, L., 2013. Late Cenozoic continuous aridification in the western Qaidam Basin: evidence from sporopollen records. Clim. Past 9, 1863–1877.
- Mii, H.S., Grossman, E.L., Yancey, T.E., Chuvashov, B., Egorov, A., 2001. Isotopic records of brachiopod shells from the Russian Platform-Evidence for the onset of mid-Carboniferous glaciation. Chem. Geol. 175, 133–147.

- Miller, K.G., Kominz, M.A., Browning, J.V., Wright, J.D., Mountain, G.S., Katz, M.E., Sugarman, P.J., Cramer, B.S., Christie-Blick, N., Pekar, S.F., 2005. The Phanerozoic record of global sea-level change. Science 310, 1293–1298.
- Montañez, I.P., Poulsen, C., 2013. The Late Paleozoic ice age: an evolving paradigm. Annu. Rev. Earth Planet. Sci. 41, 629–656.
- Montañez, I.P., Tabor, N.J., Niemeier, D., DiMichele, W.A., Frank, T.D., Fielding, C.R., Isbell, J.L., Birgenheier, L.P., Rygel, M.C., 2007. CO₂-forced climate and vegetation instability during Late Paleozoic deglaciation. Science 315, 87–91.
- Montañez, I.P., McElwain, J.C., Poulsen, C.J., White, J.D., DiMichele, W.A., Wilson, J.P., Griggs, G., Hren, M.T., 2016. Climate, pCO₂ and terrestrial carbon cycle linkages during late Palaeozoic glacial-interglacial cycles. Nat. Geosci. 9, 824–828.
- Mottin, T.E., Vesely, F.F., de Lima Rodrigues, M.C.N., Kipper, F., de Souza, P.A., 2018. The paths and timing of late Paleozoic ice revisited: New stratigraphic and paleo-ice flow interpretations from a glacial succession in the upper Itararé Group (Paraná Basin, Brazil). Palaeogeogr. Palaeoclimatol. Palaeoecol. 490, 488–504.
- Muttoni, G., Kent, D.V., Garzanti, E., Brack, P., Abrahamsen, N., Gaetani, M., 2003. Early permian pangea 'B' to late permian pangea 'A'. Earth Planet. Sci. Lett. 215, 379–394.
- Muttoni, G., Gaetani, M., Kent, D.V., Sciunnach, D., Angiolini, L., Berra, F., Garzanti, E., Mattei, M., Zanchi, A., 2009. Opening of the Neo-Tethys Ocean and the Pangea B to Pangea A transformation during the Permian. GeoArabia 14, 17–48.
- Nesbitt, H., Young, G., 1982. Early Proterozoic climates and plate motions inferred from major element chemistry of lutites. Nature 299, 715–717.
- Neumann, E.-R., Wilson, M., Heeremans, M., Spencer, E.A., Obst, K., Timmerman, M.J., Kirstein, L., 2004. Carboniferous-Permian rifting and magmatism in southern Scandinavia, the North Sea and northern Germany: a review. Geol. Soc. Lond., Spec. Publ. 223, 11–40.
- Niu, S., Hu, H., Mao, J., Sun, A., Xu, C., Hou, Q., 2004. Structure in Western Shandong and its genetic mechanism. Chinese Geol. 31, 34–39 (in Chinese with English abstract).
- Nriagu, J., Becker, C., 2003. Volcanic emissions of mercury to the atmosphere: global and regional inventories. Sci. Total Environ. 304, 3–12.
- Parker, A., 1970. An index of weathering for silicate rocks. Geol. Mag. 107, 501–504.
 Percival, L., Witt, M., Mather, T., Hermoso, M., Jenkyns, H., Hesselbo, S., Al-Suwaidi, A., Storm, M., Xu, W., Ruhl, M., 2015. Globally enhanced mercury deposition during the end-Pliensbachian extinction and Toarcian OAE: A link to the Karoo–Ferrar Large Igneous Province. Earth Planet. Sci. Lett. 428, 267–280.
- Pyle, D.M., Mather, T.A., 2003. The importance of volcanic emissions for the global atmospheric mercury cycle. Atmos. Environ. 37, 5115–5124.
- Qi, L., Cawood, P.A., Yang, J., Xu, Y., Du, Y., 2020. Quantifying temperature variation between Neoproterozoic cryochron-nonglacial interlude, Nanhua Basin, South China, Precambrian Res. 351, 105967.
- Racki, Grzegorz, Rakocinski, Michal, Marynowski, Leszek, Wignall, Paul, 2018. Mercury enrichments and the Frasnian-Famennian biotic crisis: A volcanic trigger proved? Geology 46, 543–546.
- Rasmussen, C., Brantley, S., Richter, D.D., Blum, A., Dixon, J., White, A.F., 2011. Strong climate and tectonic control on plagioclase weathering in granitic terrain. Earth Planet. Sci. Lett. 301. 521–530.
- Richey, J.D., Montañez, I.P., Goddéris, Y., Looy, C.V., Griffis, N.P., DiMichele, W.A., 2020. Influence of temporally varying weather ability on CO₂-climate coupling and ecosystem change in the late Paleozoic. Clim. Past 16, 1759–1775.
- Riebe, C.S., Kirchner, J.W., Finkel, R.C., 2004. Erosional and climatic effects on long-term chemical weathering rates in granitic landscapes spanning diverse climate regimes. Earth Planet. Sci. Lett. 224, 547–562.
- Rieu, R., Allen, P.A., Plotze, M., Pettke, T., 2007. Compositional and mineralogical variations in a Neoproterozoic glacially influenced succession, Mirbat area, south Oman: Implications for paleoweathering conditions. Precambrian Res. 154, 248–265.
- Roddaz, M., Viers, J., Brusset, S., Baby, P., Boucayrand, C., Hérail, G., 2006. Controls on weathering and provenance in the Amazonian foreland basin: insights from major and trace element geochemistry of Neogene Amazonian sediments. Chem. Geol. 226, 31-65.
- Rosa, E.L.M., Isbell, J.L., 2021. Late Paleozoic glaciation. In: Encyclopedia of Geology, Second edition.
- Rudnick, R., Gao, S., Holland, H., Turekian, K., 2003. Composition of the continental crust. Treat. Geochem. 3, 1–64.
- Sanei, H., Grasby, S.E., Beauchamp, B., 2012. Latest Permian mercury anomalies. Geology 40, 63–66.
- Sato, A.M., Llambías, E.J., Basei, M.A., Castro, C.E., 2015. Three stages in the Late Paleozoic to Triassic magmatism of southwestern Gondwana, and the relationships with the volcanogenic events in coeval basins. J. S. Am. Earth Sci. 63, 48–69.
- Scheffler, K., Hoernes, S., Schwark, L., 2003. Global changes during Carboniferous–Permian glaciation of Gondwana: Linking polar and equatorial climate evolution by geochemical proxies. Geology 31, 605–608.
- Scotese, C., 2014. Atlas of Permo-Carboniferous paleogeographic maps (Mollweide projection). The Late Paleozoic, Paleomap Atlas for ArcGIS.
- Self, S., Widdowson, M., Thordarson, T., Jay, A.E., 2006. Volatile fluxes during flood basalt eruptions and potential effects on the global environment: a Deccan perspective. Earth Planet. Sci. Lett. 248, 518–532.
- Selin, N.E., 2009. Global biogeochemical cycling of mercury: a review. Annu. Rev. Environ. Resour. 34, 43–63.
- Shao, L., Wang, H., Yu, X., Lu, J., Zhang, M., 2012. Paleo-fires and atmospheric oxygen levels in the latest Permian: evidence from maceral compositions of coals in eastern Yunnan, Southern China. Acta Geol. Sinica-English Edition 86, 949–962.
- Sheldon, N.D., 2006. Abrupt chemical weathering increase across the Permian-Triassic boundary. Palaeogeogr. Palaeoclimatol. Palaeoecol. 231, 315–321.

- Sheldon, N.D., Tabor, N.J., 2009. Quantitative paleoenvironmental and paleoclimatic reconstruction using paleosols. Earth-Sci. Rev. 95, 1–52.
- Shen, S.Z., Cao, C., Henderson, C.M., Wang, X., Shi, G.R., Wang, Y., Wang, W., 2006. End-Permian mass extinction pattern in the northern peri-Gondwanan region. Palaeoworld 15, 3–30.
- Shen, J., Algeo, T.J., Chen, J., Planavsky, N.J., Feng, Q., Yu, J., Liu, J., 2019a. Mercury in marine Ordovician/Silurian boundary sections of South China is sulfide-hosted and non-volcanic in origin. Earth Planet. Sci. Lett. 511, 130–140.
- Shen, J., Yu, J., Chen, J., Algeo, T.J., Xu, G., Feng, Q., Shi, X., Planavsky, N.J., Shu, W., Xie, S., 2019b. Mercury evidence of intense volcanic effects on land during the Permian-Triassic transition. Geology 47, 1117–1121.
- Sial, A., Lacerda, L., Ferreira, V., Frei, R., Marquillas, R., Barbosa, J., Gaucher, C., Windmöller, C., Pereira, N., 2013. Mercury as a proxy for volcanic activity during extreme environmental turnover: the Cretaceous-Paleogene transition. Palaeogeogr. Palaeoclimatol. Palaeoecol. 387, 153–164.
- Singh, P., Rajamani, V., 2001. REE geochemistry of recent clastic sediments from the Kaveri floodplains, southern India: implication to source area weathering and sedimentary processes. Geochim. Cosmochim. Acta 65, 3093–3108.
- Soreghan, G.S., Soreghan, M.J., Heavens, N.G., 2019. Explosive volcanism as a key driver of the late Paleozoic ice age. Geology 47, 600–604.
- Sun, Q., Colin, C., Chen, F., Zhang, J., 2011. A discussion on the factors affecting formation and quantity of clay minerals in climatic and environmental research. Acta Petrol. Mineral. 30, 291–300 (in Chinese with English abstract).
- Sun, S., Chen, A., Chen, H., Hou, M., Yang, S., Xu, S., Wang, F., Huang, Z., Ogg, J.G., 2022. Early Permian chemical weathering indices and paleoclimate transition linked to the end of the coal-forming episode, Ordos Basin, North China Craton. Palaeogeogr. Palaeoclimatol. Palaeoecol. 585, 110743.
- Tabor, N.J., Poulsen, C.J., 2008. Palaeoclimate across the Late Pennsylvanian–Early Permian tropical palaeolatitudes: a review of climate indicators, their distribution, and relation to palaeophysiographic climate factors. Palaeogeogr. Palaeoclimatol. Palaeoecol. 268, 293–310.
- Taylor, S.R., McLennan, S.M., 1985. The Continental Crust: Its Composition and Evolution.
- Torsvik, T.H., Smethurst, M.A., Burke, K., Steinberger, B., 2008. Long term stability in deep mantle structure: evidence from the ~ 300 Ma Skagerrak-Centered Large Igneous Province (the SCLIP). Earth Planet. Sci. Lett. 267, 444–452.
- Turner, S.K., 2018. Constraints on the onset duration of the Paleocene–Eocene thermal maximum. Philos. Trans. Royal Soc. Math. Phys. Eng. Sci. 376, 20170082.
- Vervoort, P., Adloff, M., Greene, S.E., Turner, S.K., 2019. Negative carbon isotope excursions: an interpretive framework. Environ. Res. Lett. 14, 085014.
- Wang, H., 1985. Atlas of the Palaeogeography of China. Cartographic Publishing House, Beijing, China (in Chinese with English abstract).
- Wang, J., 2010. Late Paleozoic macrofloral assemblages from Weibei Coalfield, with reference to vegetational change through the Late Paleozoic Ice-age in the North China Block. Int. J. Coal Geol. 83, 292–317.
- Wang, B., Li, X., Yuan, H., Zhou, H., Cheng, H., Jiang, W., Yan, H., 2009. Geochemical characteristics of Strontium elements in surface water environment of central and eastern China. Earth Environ. 37, 42–49 (in Chinese with English abstract).
- Wang, X., Cawood, P.A., Zhao, H., Zhao, L., Grasby, S.E., Chen, Z.-Q., Wignall, P.B., Lv, Z., Han, C., 2018. Mercury anomalies across the end Permian mass extinction in South China from shallow and deep water depositional environments. Earth Planet. Sci. Lett. 496, 159–167.
- Wang, X., Cawood, P.A., Zhao, H., Zhao, L., Grasby, S.E., Chen, Z.Q., Zhang, L., 2019. Global mercury cycle during the end-Permian mass extinction and subsequent Early Triassic recovery. Earth Planet. Sci. Lett. 513, 144–155.
- Wang, P., Du, Y., Yu, W., Algeo, T.J., Zhou, Q., Xu, Y., Qi, L., Yuan, L., Pan, W., 2020. The chemical index of alteration (CIA) as a proxy for climate change during glacialinterglacial transitions in Earth history. Earth Sci. Rev. 201, 103032.
- Wilkinson, B., 2005. Humans as geologic agents: A deep-time perspective. Geology 33, 161-164.
- Wronkiewicz, D.J., Condie, K.C., 1987. Geochemistry of Archean shales from the Witwatersrand Supergroup, South Africa: source-area weathering and provenance. Geochim. Cosmochim. Acta 51, 2401–2416.
- Wu, Q., Ramezani, J., Zhang, H., Wang, J., Zeng, F., Zhang, Y., Liu, F., Chen, J., Cai, Y., Hou, Z., 2021. High-precision U-Pb age constraints on the Permian floral turnovers, paleoclimate change, and tectonics of the North China block. Geology 49, 677–681.
- Yan, Q., Zhang, G., Li, S., Wang, H., Wu, B., Dong, R., Wang, Y., Guo, W., 1979. Transgression and sedimentary environment of Funing Group in Jinhu Sag, Northern Jiangsu province. Acta Geol. Sinica 77–99 (in Chinese with English abstract).
- Yan, Z., Shao, L., Glasspool, I., Wang, J., Wang, X., Wang, H., 2019. Frequent and intense fires in the final coals of the Paleozoic indicate elevated atmospheric oxygen levels at the onset of the End-Permian Mass Extinction Event. Int. J. Coal Geol. 207, 75–83.
- Yang, J., Cawood, P.A., Du, Y., Feng, B., Yan, J., 2014. Global continental weathering trends across the Early Permian glacial to postglacial transition: Correlating high-and low-paleolatitude sedimentary records. Geology 42, 835–838.
- Yang, J., Cawood, P.A., Du, Y., Li, W., Yan, J., 2016. Reconstructing Early Permian tropical climates from chemical weathering indices. Geol. Soc. Am. Bull. 128, 739–751.
- Yang, H., Yang, D., Shi, J., Xu, W., Wang, F., Chen, Y., 2018a. Nature of the Early Cretaceous lithospheric mantle in western Shangdong: Constraints from geochronology,geochemistry and Sr-Nd-Pb-Hf isotopic data of Dakunlun gabbros and diabases. Acta Petrol. Sin. 34, 14 (in Chinese with English abstract).
- Yang, J., Cawood, P.A., Du, Y., Condon, D.J., Yan, J., Liu, J., Huang, Y., Yuan, D., 2018b. Early Wuchiapingian cooling linked to Emeishan basaltic weathering? Earth Planet. Sci. Lett. 492, 102–111.

- Yang, J., Cawood, P.A., Montañez, I.P., Condon, D.J., Du, Y., Yan, J.-X., Yan, S., Yuan, D., 2020. Enhanced continental weathering and large igneous province induced climate warming at the Permo-Carboniferous transition. Earth Planet. Sci. Lett. 534, 116074.
- Yin, H., Feng, Q., Lai, X., Baud, A., Tong, J., 2007. The protracted Permo-Triassic crisis and multi-episode extinction around the Permian–Triassic boundary. Glob. Planet. Chang. 55, 1–20.
- Yuan, W., Yang, Z., 2015. The Alashan Terrane did not amalgamate with North China block by the Late Permian: evidence from Carboniferous and Permian paleomagnetic results. J. Asian Earth Sci. 104, 145–159.
- Zambardi, T., Sonke, J., Toutain, J., Sortino, F., Shinohara, H., 2009. Mercury emissions and stable isotopic compositions at Vulcano Island (Italy). Earth Planet. Sci. Lett. 277, 236–243.
- Zhang, L., Zhou, J., Niu, B., Wang, H., 1989. Fusulinids from Late Carboniferous Taiyuan Formation in Zibo area, Shandong. Acta Palaeontol. Sinica 28 (803-818), 839–842.
- Zhang, S., Zhao, Y., Kröner, A., Liu, X., Xie, L., Chen, F., 2009. Early Permian plutons from the northern North China Block: constraints on continental arc evolution and convergent margin magmatism related to the Central Asian Orogenic Belt. Int. J. Earth Sci. 98, 1441–1467.
- Zhang, X., Li, S., Geng, G., Wang, X., Yan, M., 2021. Discussion on some problems about the division of marine and terrestrial facies by using B content and B/Ga ratio. China Sci. Paper 16, 104–111 (in Chinese with English abstract).
- Zhao, H., Shen, J., Algeo, T.J., Racki, G., Chen, J., Huang, C., Song, J., Qie, W., Gong, Y., 2022. Mercury isotope evidence for regional volcanism during the Frasnian-Famennian transition. Earth Planet. Sci. Lett. 581, 117412.
- Zhu, Y., Zhang, J., Jia, Q., Zhang, X., Wang, M., 2005. Study on the fusulinid fauna and the Carboniferous-Permian boundary in the Taiyuan Formation from the Yanzhou Coalfield, Shandong, Province. Acta Morphol. Sinica 22, 12 (in Chinese with English abstract)